

Reconstruction of LiF-rich interphases through an anti-freezing electrolyte for ultralow-temperature LiCoO₂ batteries

Jipeng Liu,^{‡abc} Botao Yuan,^{‡a} Niandong He,^a Liwei Dong,^b Dongjiang Chen,^a Shijie Zhong,^a Yuanpeng Ji,^b Jiecai Han,^a Chunhui Yang,^{bc} Yuanpeng Liu^{*a} and Weidong He^{*a}

^aNational Key Laboratory of Science and Technology on Advanced Composites in Special Environments, and Center for Composite Materials and Structures, Harbin Institute of Technology, Harbin 150080, China

^bMIIT Key Laboratory of Critical Materials Technology for New Energy Conversion and Storage, School of Chemistry and Chemical Engineering, Harbin Institute of Technology, Harbin 150001, China

^cState Key Laboratory of Urban Water Resource and Environment, Harbin Institute of Technology, Harbin 150001, China

Corresponding Author

*E-mail: liuyp@hit.edu.cn, weidong.he@hit.edu.cn

‡These authors have contributed equally.

Experimental section

Materials. Lithium difluoro (oxalato) borate (LiDFOB, 99.9%), fluoroethylene carbonate (FEC, 99.9%), 1 M lithium hexafluorophosphate (LiPF₆, 99.9%) in ethylene carbonate (EC, 99.9%)/dimethyl carbonate (DMC, 99.9%) (v/v=1:1), LiCoO₂ (LCO, 99.9%), LiNi_{0.8}Co_{0.1}Mn_{0.1}O₂ (NCM811, 99.9%), LiNi_{0.8}Co_{0.15}Al_{0.05}O₂ (NCA, 99.9%), LiFePO₄ (LFP, 99.9%), carbon black (99.9%) and poly (vinylidene fluoride) (PVDF, 99.9%) and N-methyl-2-pyrrolidone (NMP, 99.5%) were obtained from Guangdong Canrd New Energy Technology Co.,Ltd. Dimethyl sulfite (DMS, 99.0%) and Iso-butyl formate (IF, 97.0%) were purchased from Adamas-beta® and dehydrated with 4 Å molecular sieve for 12 hours.

Preparation of electrolytes. The LiDFOB was dried under vacuum at 60 °C for 12 h. For the typical 1M LiDFOB-FEC/DMS/IF electrolyte, 20 vt.% FEC was a constant volume and volume ratios of IF were 40%, 45%, 50%, 60%, and 70%, respectively. 1 M LiDFOB in 50 vt.% FEC and 50 vt.% DMS was selected as one of the reference electrolytes, named as FEC+DMS. The commercial electrolyte of 1 M LiPF₆ in EC/DMC (v/v=1:1) was chosen as another reference electrolyte, named as EC+DMC.

Characterizations. The freezing points of the electrolytes were determined by the first-order transition of the temperature-related magnetic susceptibility under the magnetic property measurement system¹ (Quantum Design, MPMS XL 5, U.S.A.) with 1 °C min⁻¹ scanning rate. Differential scanning calorimetry (DSC) was assisted with MPMS in determining the freezing point of the electrolytes (Netzsch, DSC 200F3, U.S.A.) from 25 °C to -150 °C. The apparent viscosity was measured with rotational viscosity test

(Thermofisher, Thermo HAAKE MARS 60, U.S.A.) at various temperatures. Thermogravimetry (TG) was analyzed with a synchronous thermal analyzer (Netzsch, TGA5500, Germany). The wetting angles of the electrolytes on separator were measured with an automatic contact angle measuring instrument (ZhongChen, JC2000D3M, China). The low-temperature electrochemical performances were measured in a low-temperature test chamber (Hebei Huida, DW-80, China). The morphology of the Li metal anodes after cycling with various electrolytes was characterized with scanning electron microscopy (Zeiss, Zeiss Supra 55, Germany) and optical digital microscopy (Olympus, DSX-HRSU, U.S.A.). The cross-sectional morphology of electrochemically deposited Li metal anode was investigated by cryogenic focused ion beam electron microscopy (FEI, Helios Nanolab 600i, U.S.A.). The cross-sections were firstly rough milled with a cross-sectional cut (30 kV, 21 nA) followed by a cross-sectional cleaning cut (30 kV, 0.79 nA). Raman spectra and FT-IR spectra of different electrolytes, solvents and lithium salts were presented on a 532nm laser Raman spectrometer (Renishaw, inVia, U.K) and FTIR instrument (Nicolet, is50, U.S.A.). The cells with EC+DMC and 45% IF electrolytes were disassembled in an Argon glovebox after the fiftieth cycle at -20 °C. The interfacial compositions of the Li metal anodes and various cathodes after cycling were studied by XPS (Thermo-Fisher, ESCALAB 250Xi, U.S.A.) and TOF-SIMS (ION-TOF GmbH, Ion tof Gmhb 5, Germany). The electrolytes were dissolved in 1 mL CDCl₃-d₁ for 5 minutes. The Nuclear Magnetic Resonance (NMR) spectra were recorded on a NMR spectrometer

(Bruker, Bruker Avance 400M, Germany). ^1H and ^{13}C NMR spectra were internally referenced to $\text{CDCl}_3\text{-d}_1$ at 7.26 and 77.00 ppm, respectively.

Electrochemical Measurements. For the fabrication of electrodes, 80 wt.% active materials (LCO, NCM811, NCA and LFP), 10 wt.% carbon black, and 10 wt.% PVDF binder in NMP were employed to form homogeneous slurries. Then the slurries were spread on round Al foils in a diameter of 14 mm and dried at 80 °C in vacuum for 24 h. The active material loadings of the various electrodes were $\sim 3 \text{ mg cm}^{-2}$ and $\sim 10 \text{ mg cm}^{-2}$ and the amounts of the electrolytes were 50 μL and 75 μL for the electrodes of different loadings. The separator was Celgard 2320 with the diameter of 16 mm. The electrolytes were assembled into CR2025 coin-type cells for electrochemical tests. For the low-temperature and high-temperature tests, all batteries were charged and discharged at the same temperature, rather than being charged at room temperature followed by special temperature discharged in order to simulate battery practical applications. All cells were charged and discharged at a current density of 1/15 C in the initial two cycles for activation at room temperature. The battery tests at room temperature were performed on the Neware battery cycler (Neware, CT-4008T-5V20mA-164, China), and the battery tests at low temperatures and high temperatures were tested on LANHE battery cycler (LANHEC, T2001A, China), within the voltage range of 2.70-4.45 V (vs. Li^+/Li) for Li || LCO cells, within the voltage range of 3.0-4.4 V (vs. Li^+/Li) for Li || NCM811 cells and Li || NCA cells, and within the voltage range of 2.5-4.2 V (vs. Li^+/Li) for Li || LFP cells. Symmetric Li || Li cells were assembled to investigate the cyclability of Li metal in the 45% IF and EC+DMC electrolytes with a

cycling capacity of 0.5 mAh cm⁻² at a current density of 0.5 mA cm⁻² for each plating/stripping process. Nyquist plots for the impedances of various electrolytes at different temperatures were tested in a frequency range from 0.10 Hz to 1.0 MHz (Shanghai Chenhua, CHI 760e, China). The cyclic voltammograms of Li || LCO cells were tested at a scan rate of 0.1 mV s⁻¹ from 2.7 V to 4.6 V. Nucleation over-potentials in the Li || Cu cells were measured by depositing 0.5 mAh cm⁻² of Li onto the Cu current collector at 0.5 mA cm⁻² at 25 °C and -20 °C, respectively. The oxidation stabilities of various electrolytes were evaluated using linear scan voltammetry on stainless steel and Li metal electrodes at a scan rate of 0.5 mV s⁻¹ from 3.0 V to 7.0 V at 25 °C and -20 °C.

The Li⁺ transference number (t_{Li^+}) was calculated according to the Bruce-Vincent-Evans equation² (Eq. 1):

$$t_{Li^+} = \frac{I_S(\Delta V - I_0 R_0)}{I_0(\Delta V - I_S R_S)} \quad (1)$$

where ΔV is the polarization potential of 10 mV, I_0 and R_0 are the initial current and initial interfacial resistances, I_S and R_S are steady-state current and steady-state interfacial resistances after potential polarization.

The ionic conductivity was calculated based on the equation (Eq. 2):

$$\sigma = \frac{L}{SR_e} \quad (2)$$

where L is the fixed distance of 1 cm, S is the area of two platinum electrode of 1 cm² and R_e is the Ohmic resistance.

The Li⁺ conductivity of electrolyte/electrode interfaces in the 45% IF electrolyte was defined according to the equations (Eqs.3-4):

$$\sigma = (1 - \alpha)\sigma_1 + \alpha\sigma_{LiF} \quad (3)$$

$$\sigma = (1 - \beta)\sigma_2 + \beta\sigma_{LiF} \quad (4)$$

where σ_1 and σ_2 are the Li⁺ conductivities of electrolyte/anode and electrolyte/cathode interphases in commercial electrolyte at -20 °C, respectively, σ_{LiF} is the ion conductivity of LiF, and α and β denote the increased ratio of LiF groups after introducing FEC for electrolyte/anode and electrolyte/cathode interfaces, respectively.

The diffusion coefficient of Li⁺ (D_{Li^+}) was calculated based on the equations (Eq.5-6):

3-5

$$D_{Li^+} = \frac{R^2 T^2}{2A^2 n^4 F^4 C^2 \sigma^2} \quad (5)$$

$$Z' = R_D + R_L + \sigma \omega^{-1/2} \quad (6)$$

where D_{Li^+} represents the diffusion coefficient of Li⁺, R is the gas constant, T is the absolute temperature, A is the surface electrode area, n is the number of electrons per molecule during oxidization, F is the Faraday constant, C is the concentration of Li⁺, and σ is the Warburg factor, related to Z' through Eq.6 and its value can be obtained from the slope of the lines between Z' and $\omega^{-1/2}$ as shown in Fig. S52 (ESI†).

The Arrhenius equation was applied to determine the diffusion coefficient of electrolyte/anode interface in commercial electrolyte at -20 °C⁶ based on the equation (Eq.7):

$$D_{Li+,1} = D_{ref} \exp\left[-\frac{E_{act,D_i}}{R} \left(\frac{1}{T_{ref}} - \frac{1}{T}\right)\right] \quad (7)$$

where R is the universal gas constant, D_{ref} is the reference Li^+ diffusion coefficient in each SEI species, and E_{act} is the corresponding activation energy.

The diffusion coefficient of electrolyte/anode interface in the 45% IF electrolyte at -20 °C was defined according to the equation (Eq.8):

$$D_{Li+} = (1 - \alpha)D_{Li+,1} + \alpha D_{Li+,LiF} \quad (8)$$

where $D_{Li+,1}$ is the diffusion coefficient of electrolyte/anode interface in commercial electrolyte at -20 °C, $D_{Li+,LiF}$ is the diffusion coefficient of LiF, and α denotes the increased ratio of LiF groups after introducing FEC.

Lattice misfit calculation. The lattice misfits of LiF-LCO, LiF-NCM811, LiF-NCA, and LiF-LFP were defined according to the equation (Eq. 9):

$$\delta = \frac{a_s - a_f}{a_f} \times 100\% \quad (9)$$

where a_s and a_f are substrate cell parameters and epitaxial cell parameters, respectively, and δ is the lattice misfit.

Electrolyte uptake test. The electrolyte uptake was calculated by the following equation (Eq. 10):

$$\text{Electrolyte uptake (\%)} = \frac{m_{wet} - m_{dry}}{m_{dry} * \rho_{electrolyte}} \times 100\% \quad (10)$$

where m_{wet} and m_{dry} represent the weight of wet and dry separators, respectively. $\rho_{electrolyte}$ represents the electrolyte density. To eliminate the influence of different

electrolyte densities, the mass of the dry separator was multiplied by the electrolyte density to obtain the corresponding reference mass. In every 5 minutes, the mass of the wet separator with adsorbed electrolyte was weighed and divided by the reference mass to obtain the electrolyte uptake percentage.

In-situ Raman Spectroscopy. *In-situ* Raman measurements were taken by Renishaw InVia Raman microscopy with a 532 nm laser, which irradiates the electrolyte through modified negative case and Li metal foil with a 5 mm hole. The batteries were assembled in an argon-filled glove box with oxygen and water levels both below 0.01 ppm. After aging treatment, galvanostatic measurements were performed at 1/3 C within the voltage range of 2.70-4.45 V for Li || LCO cells while the Raman signals were recorded simultaneously.

Density functional theory (DFT) calculations. The HOMO and LUMO values of EC, DMC, FEC, DMS, and IF molecules were calculated with Dmol³ package. The absorption energies of solvent molecules and Li⁺ were calculated using DFT implemented with the Dmol³ package. The Perdew-Burke-Ernzerhof (PBE) exchange-correlation functional within the generalized gradient approximation (GGA) was used to describe the exchange-correlation energy. The adsorption energy was calculated with the equation: $E = E_{a-b} - (E_a + E_b)$, where E is the adsorption energy, and E_{a-b} is the total energy of the relaxed a and b models at the equilibrium state. E_a and E_b are the self-consistent field (SCF) calculation energy values of geometry-optimized a and b models. Electron exchange correlation was constructed by Perdew-Burke-Ernzerhof (PBE) function with generalized gradient approximation (GGA).

The adsorption energies between LiF and various electrodes based on the DFT were performed using Cambridge Serial Total Energy Package (CASTEP). The Perdew-Burke-Ernzerhof (PBE) exchange-correlation functional within the generalized gradient approximation (GGA) was used to describe the exchange-correlation energy. The projector-augmented-wave (PAW) method was adopted for the pseudopotentials. The energy cutoff for the plane wave basis expansion was set to 450 eV. The sampling in the Brillouin zone was set with $2 \times 3 \times 1$ by the Monkhorst-Pack method. LiF molecules were adsorbed on (1 0 4) surfaces of LCO, NMC811, NCA and (0 1 0) surface of LFP, which were modeled by a slab containing several atom layers.

The reaction energies were calculated through DFT with Becke's three parameters (B3) exchange functional in Lee-Yang-Parr (LYP) nonlocal correlation functional (B3LYP). All the geometry optimizations were proceeded with B3LYP/6-31+G(d,p) level. The energy calculations were performed at B3LYP/6-311+ +G(3df,3dp) level for more accurate calculation. The reaction energy was calculated with the equation: $E_R = E_{product} - E_{reactant}$, where E_R is the reaction energy, $E_{product}$ is the total energy value of all products, and $E_{reactant}$ is the total energy value of all reactants.

The desolvation energies of $Li^+ (anion)_m(solvent)_n$ complexes were calculated using DFT implemented with the Dmol³ package. The Perdew-Burke-Ernzerhof (PBE) exchange-correlation functional within the generalized gradient approximation (GGA) was used to describe the exchange-correlation energy. The desolvation energies were calculated with the equation:

$$E_D = E_{Li^+ (anion)_m(solvent)_n} - (E_{Li^+} + E_{(anion)_m(solvent)_n})$$

where E_D is the desolvation energy, $E_{Li^+(anion)_m(solvent)_n}$ is the total energy of the solvation structure, E_{Li^+} is the energy of Li^+ , and $E_{(anion)_m(solvent)_n}$ is energy of the solvation structure without Li^+ .

The charges of oxygen atoms in FEC, DMS and IF solvents were calculated through the Charge Model 1A (CM1A) model. The method of a multilinear transformation of the Mulliken charges was adopted to calculate atomic charges in the simulation.

MD calculations. MD simulations were conducted on the electrolytes using the LAMMPS simulation package. Optimized potentials for liquid simulations (OPLS-AA)^{7, 8} parameters and charges were generated and calculated by the LigParGen^{9, 10} for the solvent molecules. The parameters for DFOB⁻ were taken from previous publications.¹¹ For 1 M $LiPF_6$ in EC/DMC (v/v = 1:1) electrolyte, 100 $LiPF_6$, 600 EC, and 600 DMC were dissolved into a periodic box, while for 1 M $LiDFOB$ in 45% IF electrolyte, 100 $LiDFOB$, 200 FEC, 400 DMS, and 400 IF molecules were calculated. The systems were set up initially with simulation boxes of 50 Å in length, with the salt and solvent molecules distributed in the simulation boxes using Packmol.¹² First, NPT runs were performed at 300 K for 5.0 ns to ensure that the equilibrium salt dissociation had been reached. Then, the NPT runs were 3.0 ns long at 253 K and the last 2.0 ns were used to obtain the structure of the electrolyte. The solvation shell structure of Li^+ was determined by analyzing the radial distribution function (RDF) and the coordination number (CN) in the MD trajectory. The migration pathway and migration rate of Li^+ were identified from topology analysis with a MD trajectory simulation.

Phase field calculations. Phase field simulations were conducted to investigate thermodynamic behaviors during lithium electroplating using Multiphysics Object-Oriented Simulation Environment (MOOSE). The size of the simulated model was $100 \mu\text{m} \times 100 \mu\text{m}$. The Li metal anode conductivity and temperature were set as 10^7 S/m and 253 K , respectively. The conductivities and diffusion coefficients of Li^+ in the different electrolytes were set the same as the values listed in Table S4 (ESI[†]). The mode of anisotropy was 4 based on lithium cubic crystal structure and the strength of interfacial anisotropy was 0.05. The maximum mesh size was set as $8.3 \mu\text{m}$ and Dirichlet boundary conditions were applied to solve the calculation model.

The temporal evolution of the phase field order parameter is expressed as:

$$\frac{\partial \xi}{\partial t} = -L_\sigma(g'(\xi) - \kappa \nabla^2 \xi) - L_\eta h'(\xi) \left\{ \exp\left[\frac{(1-\alpha)nF\eta}{RT}\right] - c \exp\left[\frac{-\alpha nF\eta}{RT}\right] \right\} \quad (11)$$

where L_σ and L_η are the interfacial mobility and electrochemical reaction kinetic coefficient, respectively. $g(\xi)$ denotes a double well function to describe the two equilibrium states for the anode and the electrolyte. $h(\xi)$, κ , α , n , t , F , R and T are the interpolating function, the gradient coefficient, the charge transfer coefficient, the number of transfer electrons, the evolution time, the Faraday constant, the gas constant and temperature, respectively. The partial differential equation describing the lithium ion concentration c is given as:

$$\frac{\partial c}{\partial t} = \nabla(D^{eff} \nabla c + \frac{D^{eff} n F c}{RT} \nabla \phi) - \frac{c_s \partial \xi}{c_0 \partial t} \quad (12)$$

where $D^{eff} = D_s h(\xi) + D_l (1 - h(\xi))$ is the effective diffusion coefficient. D_s and D_l are the lithium ions diffusion coefficients of the solid electrolyte and the lithium anode, respectively. The electrostatic potential based on the Poisson equation is expressed as:

$$\nabla(\sigma^{eff}\nabla\phi) = nFc_s\frac{\partial\xi}{\partial t} \quad (13)$$

where $\sigma^{eff} = \sigma_s h(\xi) + \sigma_l(1 - h(\xi))$ is the effective conductivity, and σ_s and σ_l are the conductivities of the solid electrolyte and the lithium anode, respectively. The phase field model (Eqs. 11-13) is solved using the open source MOOSE framework under Dirichlet boundary conditions ($c=0$ at the left side and $c=1$ at the right side).

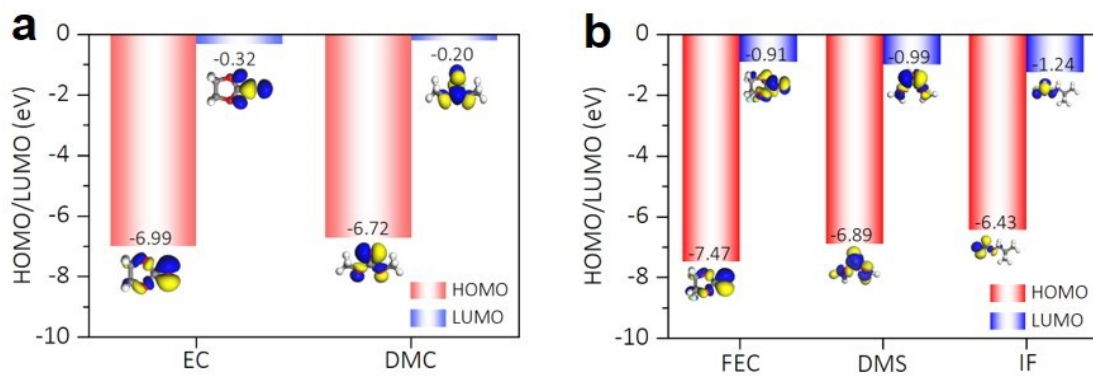


Fig. S1 HOMO and LUMO values of (a) EC, DMC, FEC, (b) DMS, and IF.

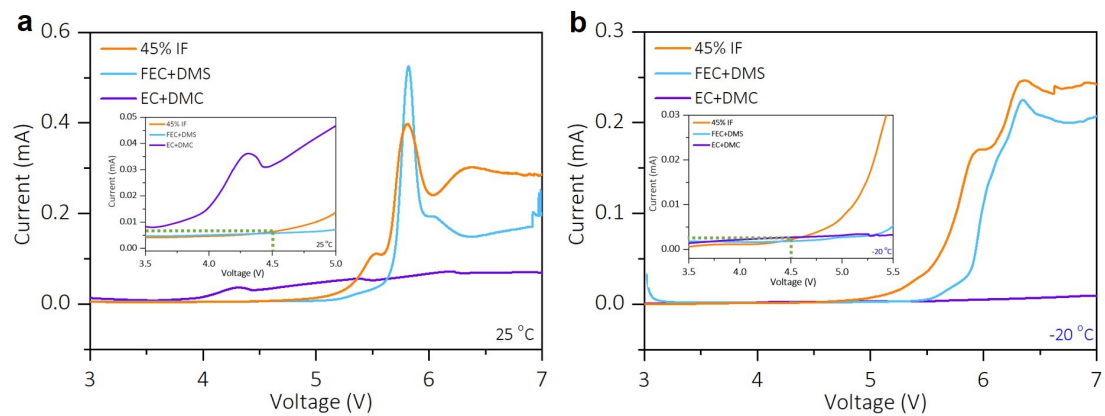


Fig. S2 The stable electrochemical windows of different electrolytes as evaluated through linear scan voltammetry measurement at (a) 25 °C and (b) -20 °C with a scan rate of 0.5 mV s⁻¹.

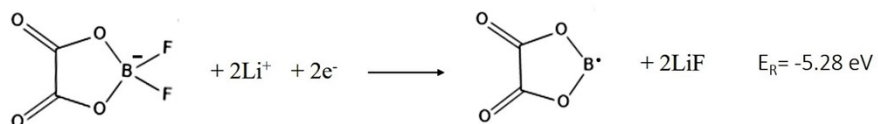
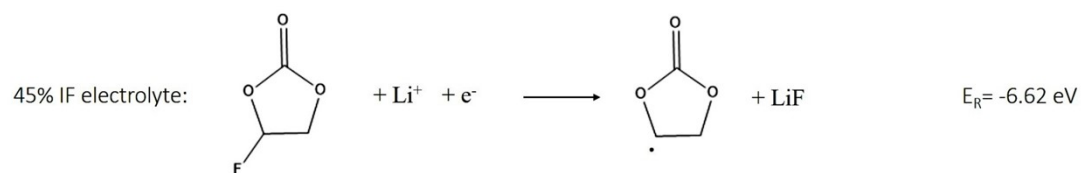


Fig. S3 Decomposition reactions of FEC, DFOB⁻ and PF₆⁻ molecules and corresponding reaction energies.

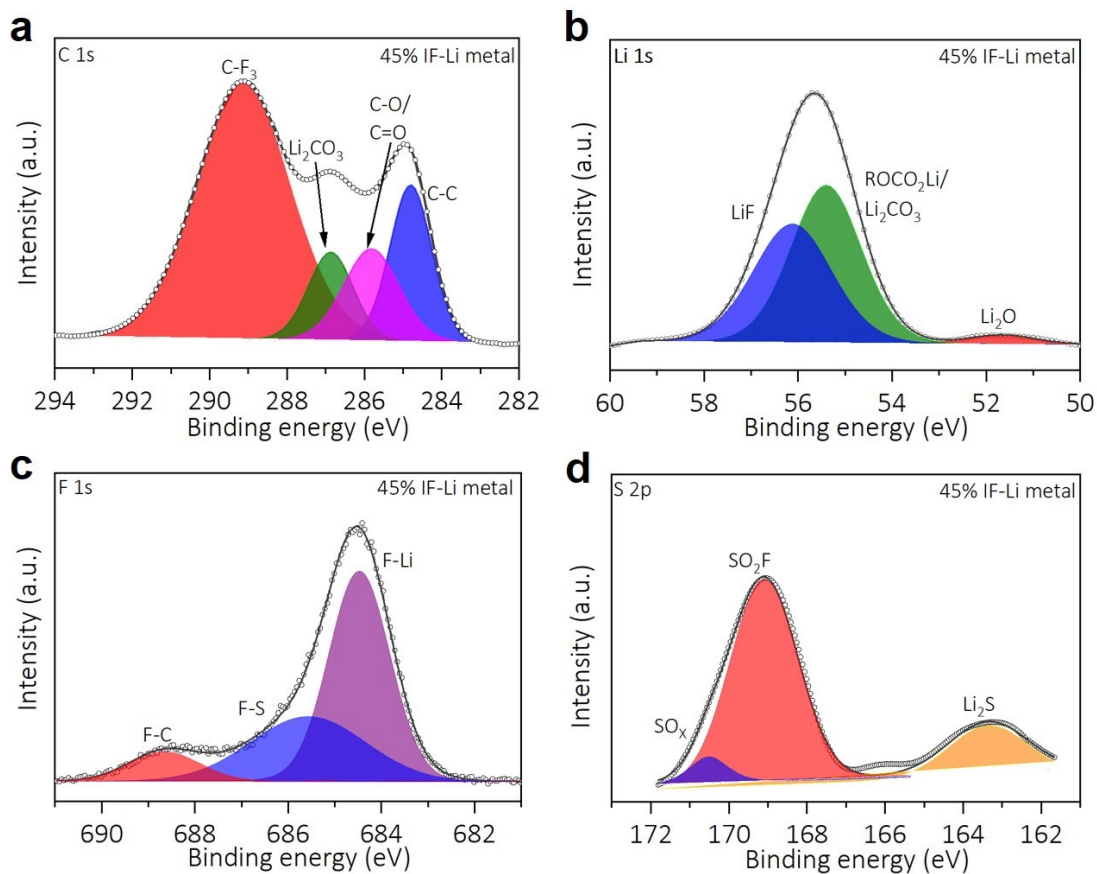


Fig. S4 XPS of the SEI interface with the 45% IF electrolyte at -20 °C. (a) C 1s, (b) Li 1s, (c) F 1s, and (d) S 2p spectra with assigned peaks through Gaussian/Lorentzian product peak fittings.

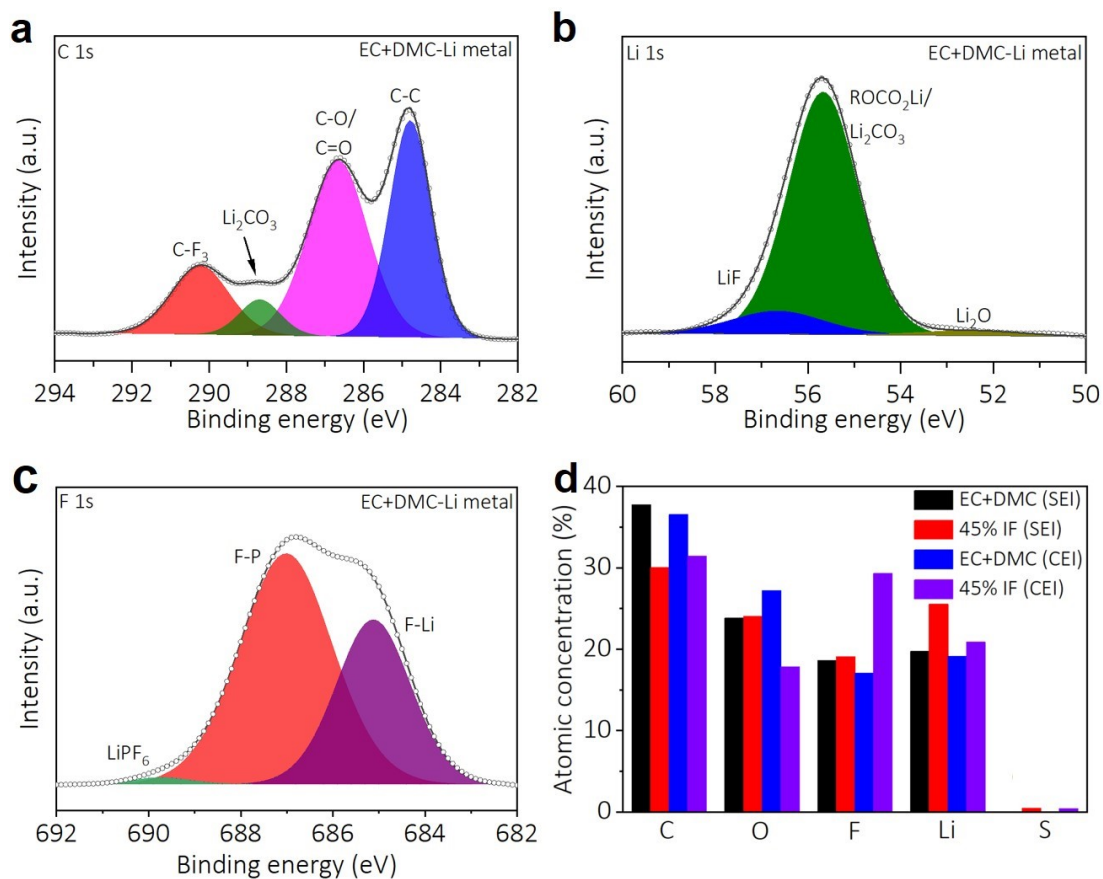


Fig. S5 XPS of the SEI interface with the EC+DMC electrolyte at -20 °C. (a) C 1s, (b) Li 1s and (c) F 1s spectra with assigned peaks through Gaussian/Lorentzian product peak fittings. (d) Compositions of SEI and CEI on the cycled electrodes in different electrolytes.

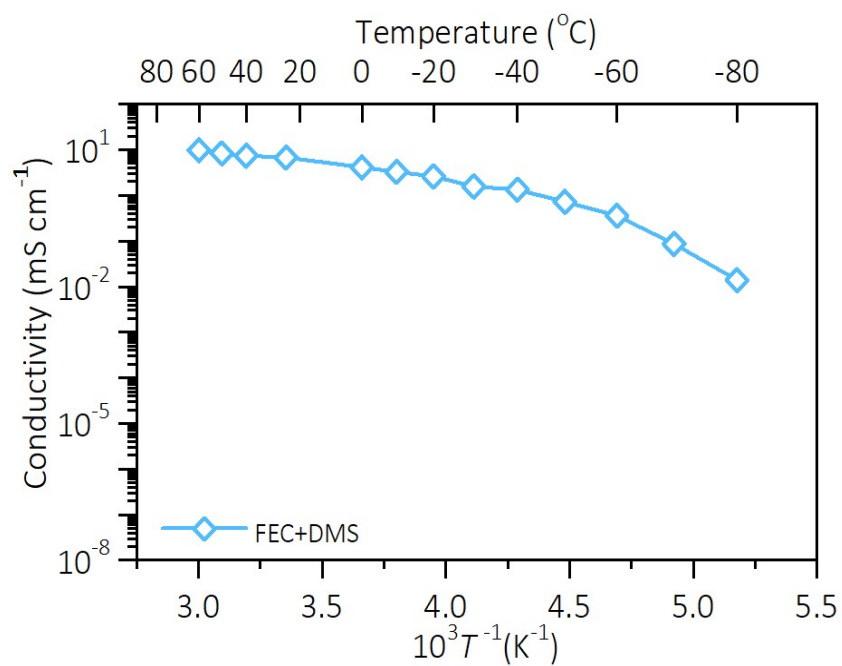


Fig. S6 Ionic conductivities of the FEC+DMS electrolyte at different temperatures.

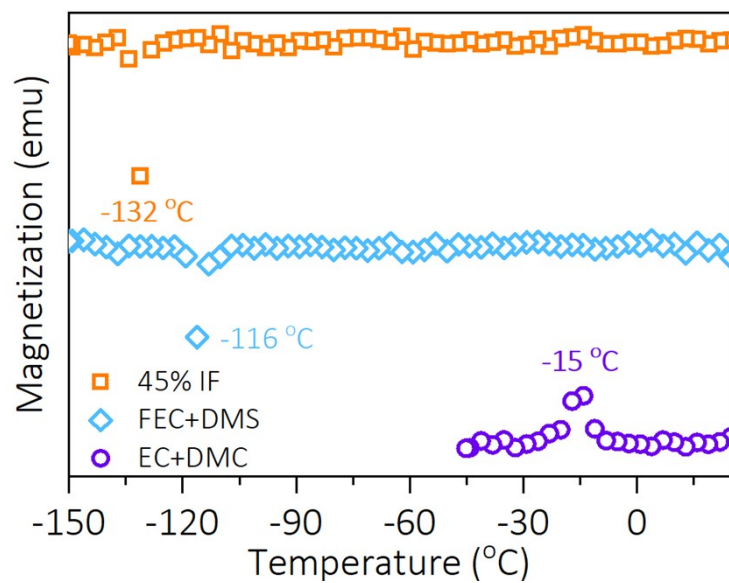


Fig. S7 Temperature dependence of the magnetic moment of the different electrolytes measured in magnetic measuring system in an applied field of 1 mT.

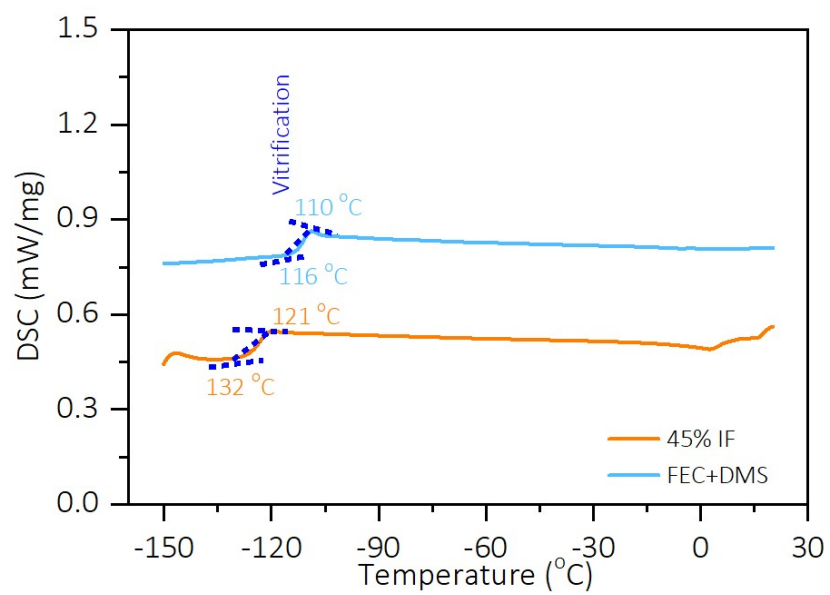


Fig. S8 DSC curves of 45% IF and FEC+DMS electrolytes.

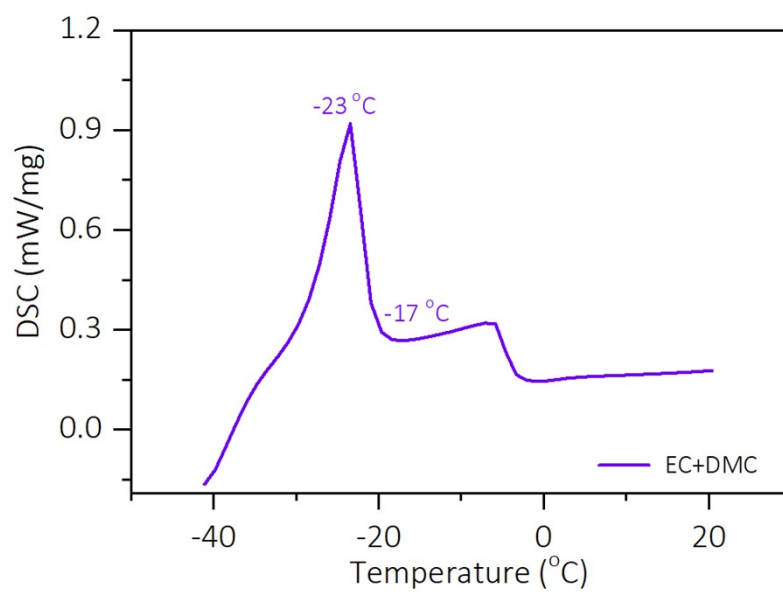


Fig. S9 DSC curve of the EC+DMC electrolyte.

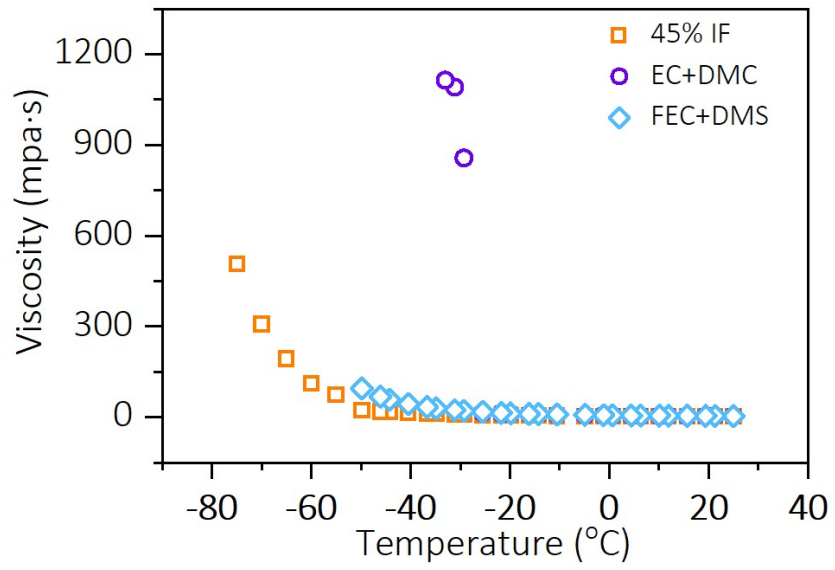


Fig. S10 Viscosity of different electrolytes with temperature ranging from 25 °C to -70 °C.

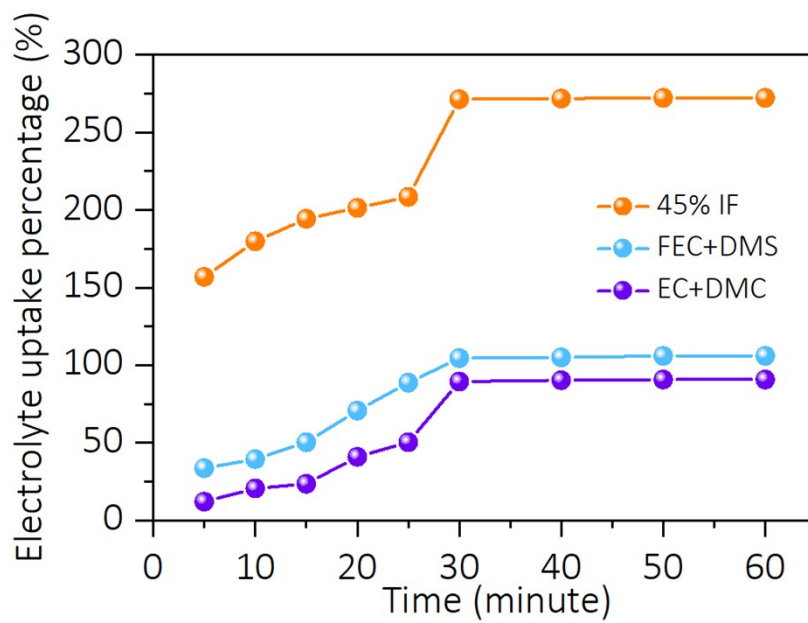


Fig. S11 Uptake curves of different electrolytes over time.

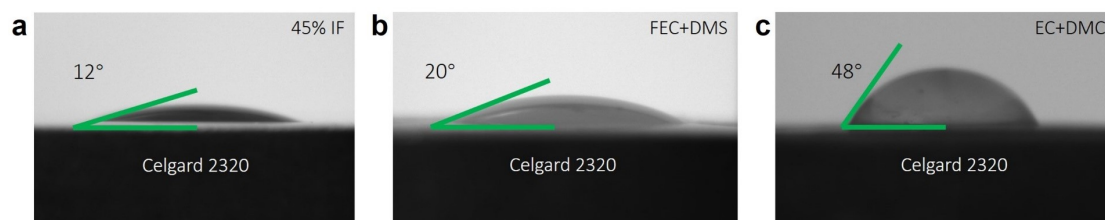


Fig. S12 Contact angles between Celgard 2320 separator and different electrolytes.

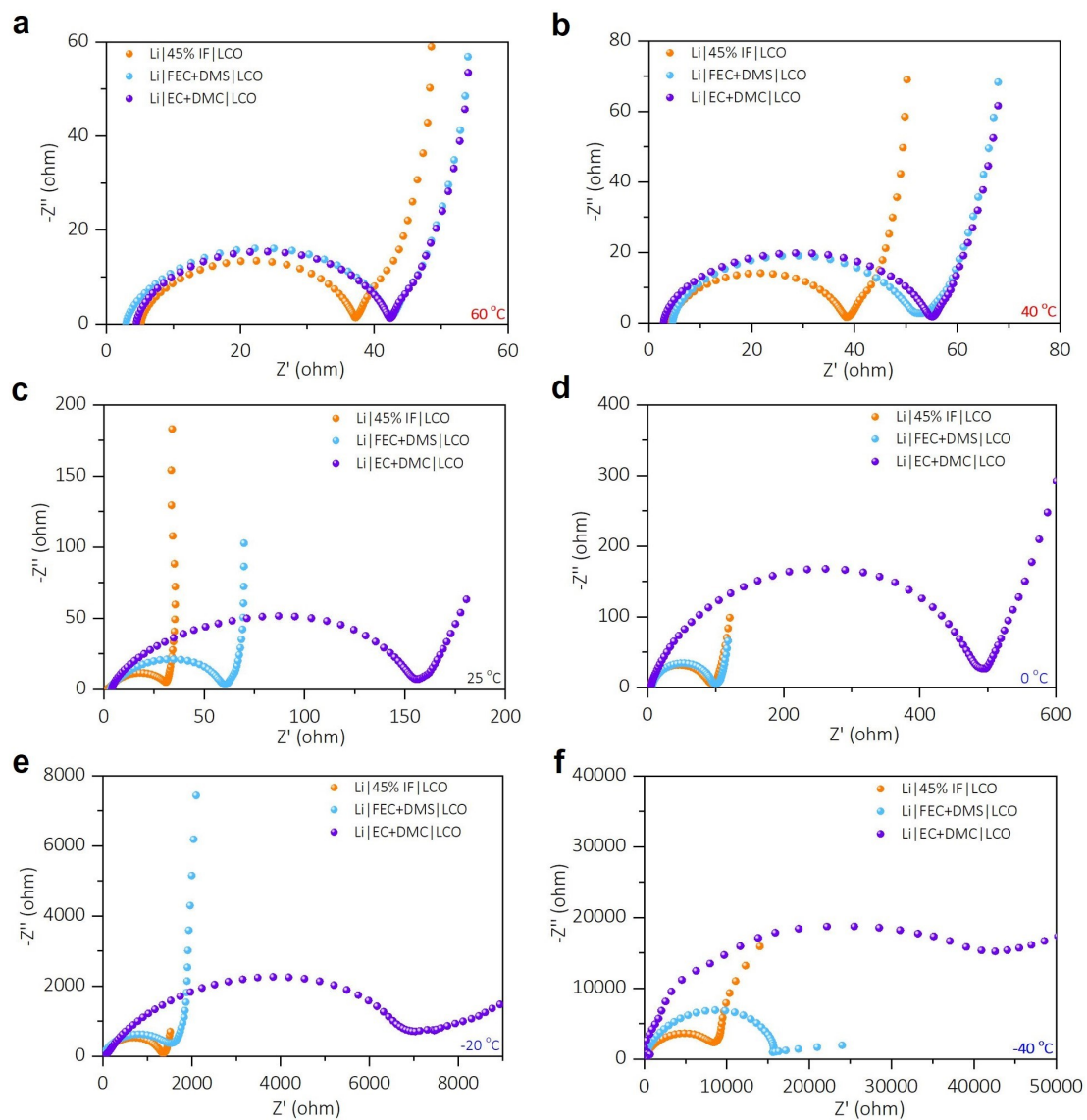


Fig. S13 EIS investigations of Li || LCO cells at various temperatures, (a) 60 °C, (b) 40 °C, (c) 25 °C, (d) 0 °C, (e) -20 °C, (f) -40 °C.

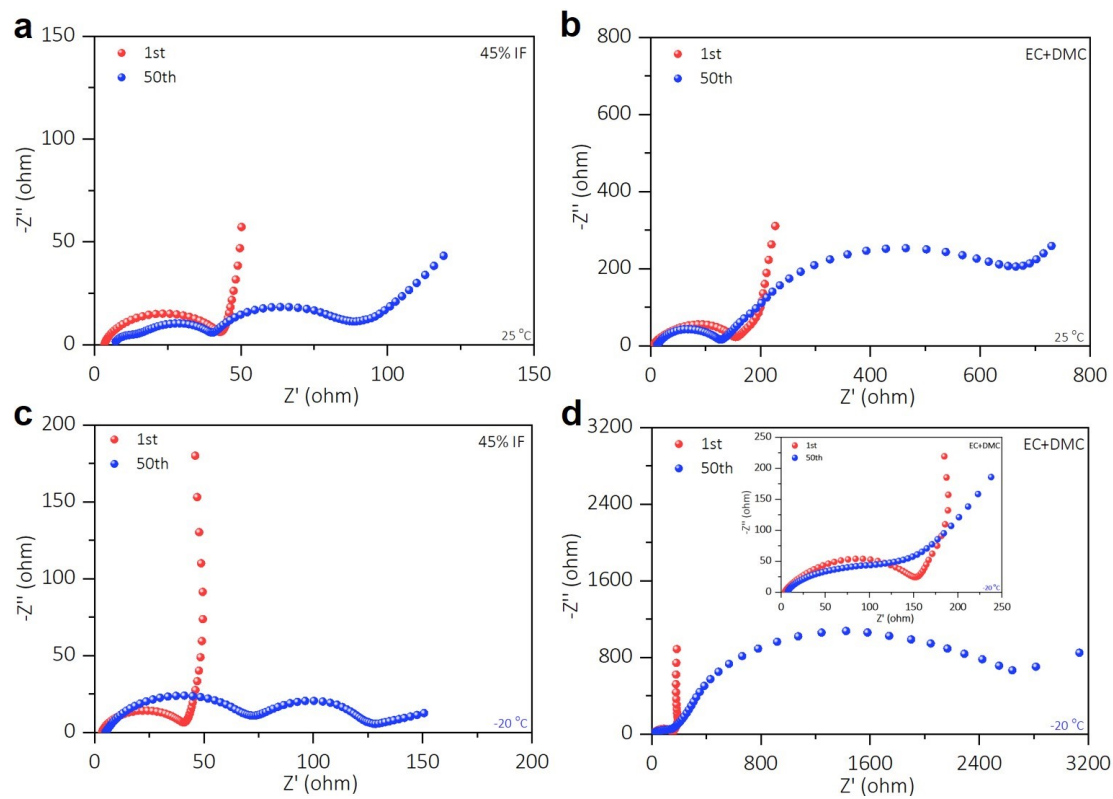


Fig. S14 Nyquist plots of the Li || LCO cells with (a) 45% IF and (b) EC+DMC electrolytes at 25 °C and (c) 45% IF and (d) EC+DMC electrolytes at -20 °C after 1st and 50th cycles at 1/3 C.

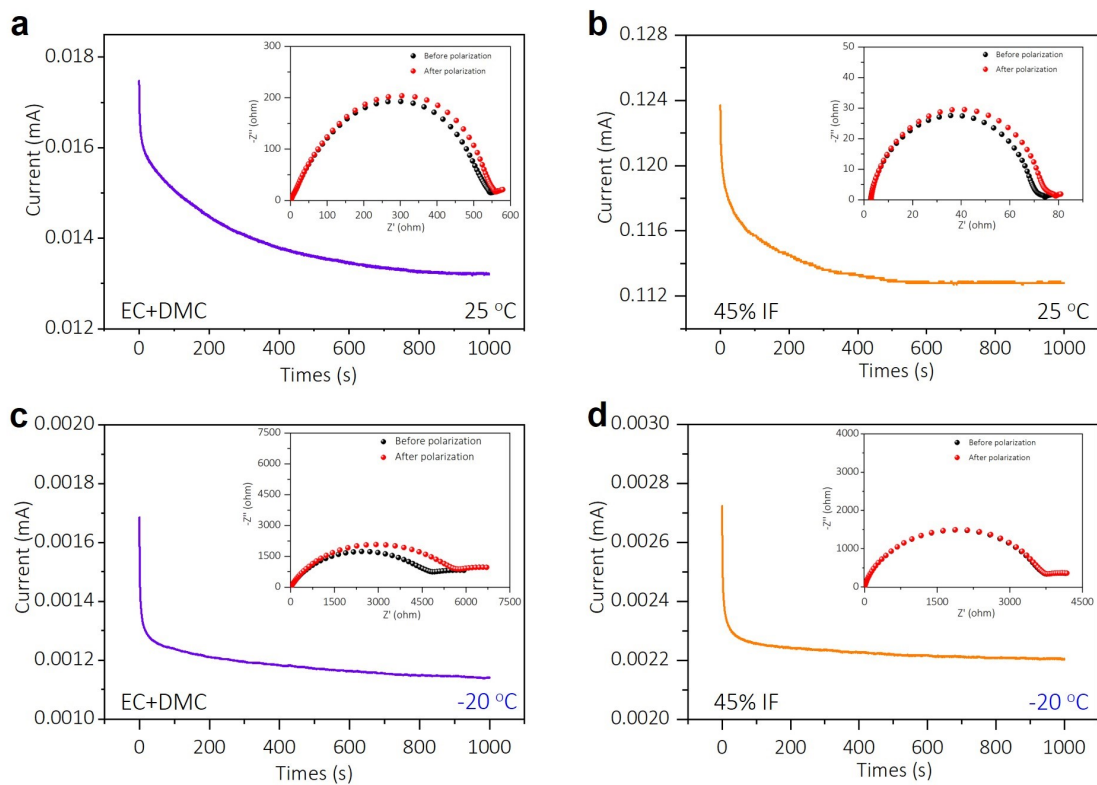


Fig. S15 Current time profiles of the symmetrical Li || Li cells with (a) EC+DMC, (b) 45% IF electrolytes at 25 °C and (c) EC+DMC, (d) 45% IF electrolytes at -20 °C (the inset shows the Nyquist impedance spectra of the batteries before and after polarization).

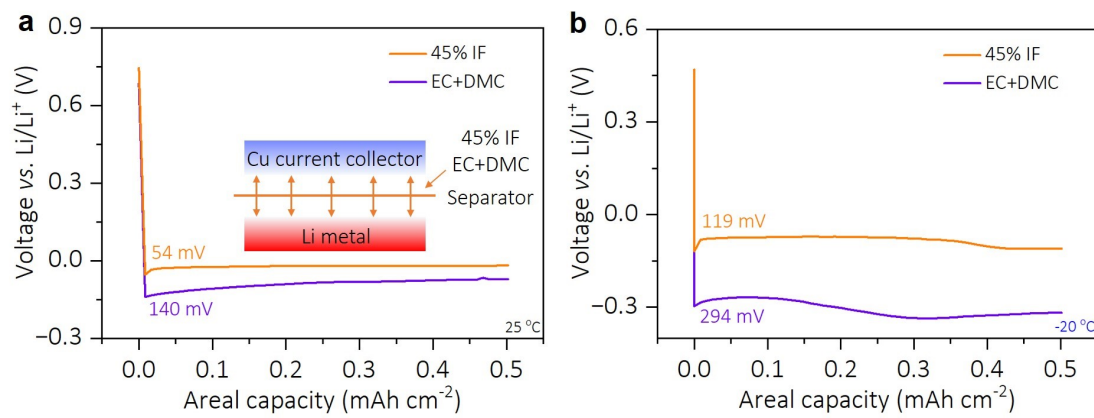


Fig. S16 Nucleation over-potentials of 45% IF and EC+DMC electrolytes at (a) 25 °C and (b) -20 °C.

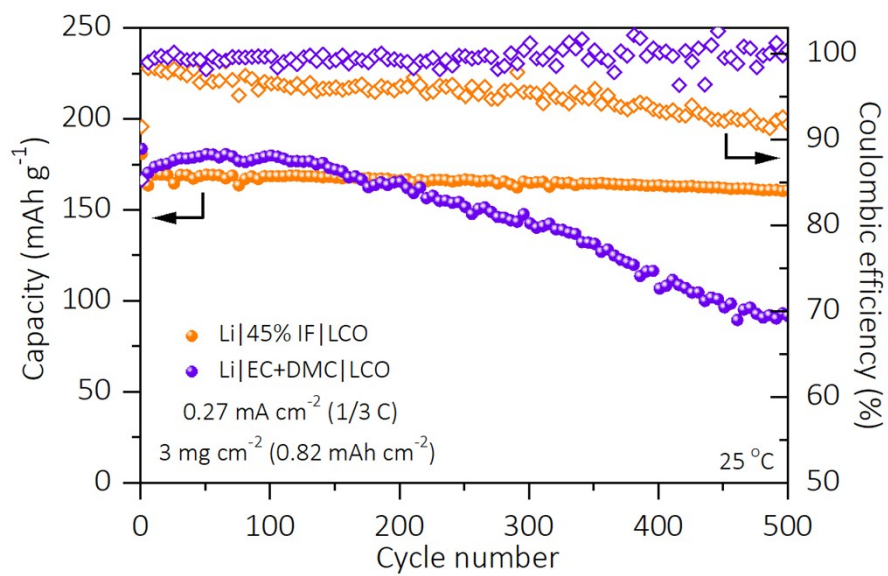


Fig.S17 Cycling performances of the Li || LCO cells with 45% IF and EC+DMC electrolytes at 1/3 C and 25 °C with a LCO loading of ~3 mg cm⁻².

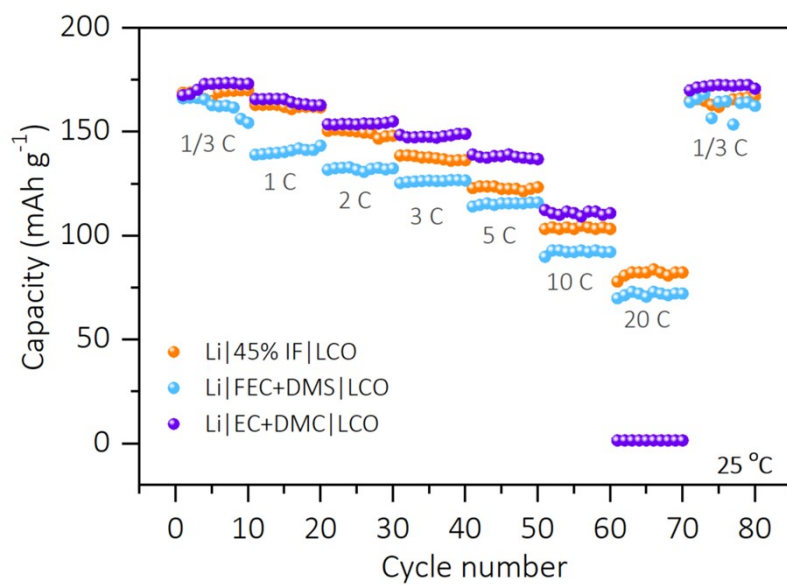


Fig. S18 Rate performances of Li || LCO cells with 45% IF, FEC+DMS, and EC+DMC electrolytes at 25 °C with a LCO loading of ~3 mg cm⁻².

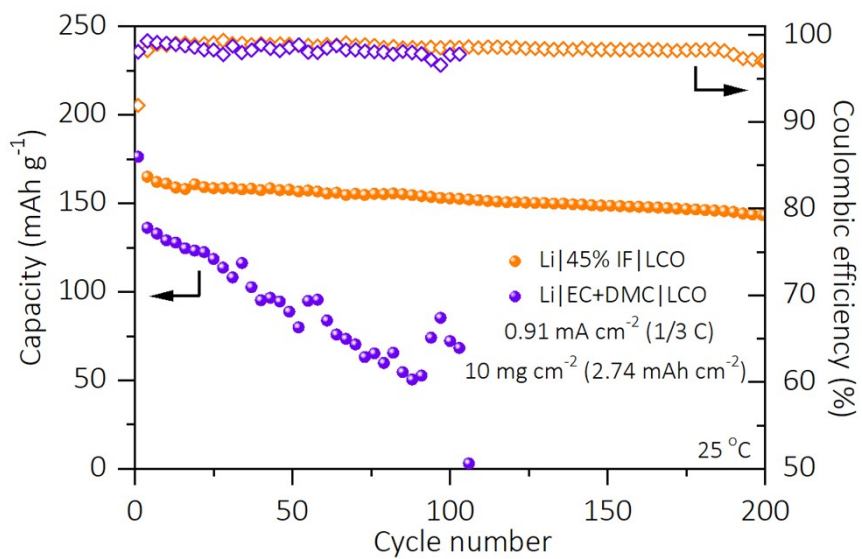


Fig. S19 Cycling performances of Li || LCO cells with 45% IF and EC+DMC electrolytes at 1/3 C and 25 °C with a LCO loading of ~10 mg cm⁻².

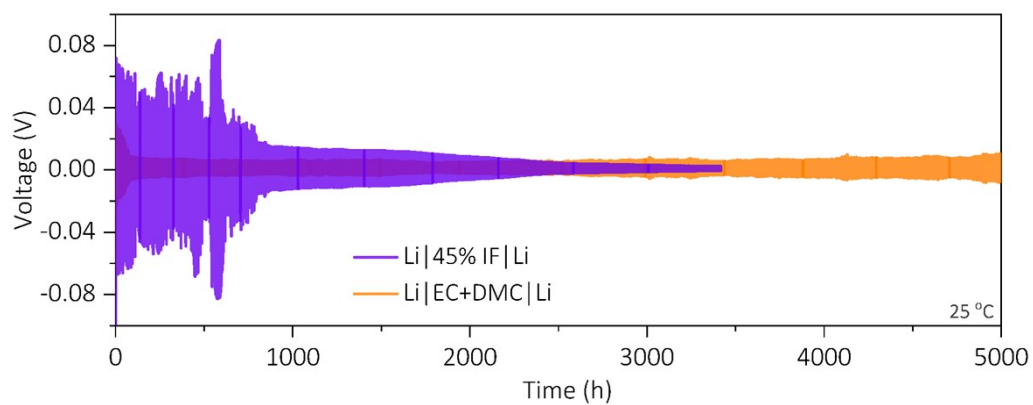


Fig. S20 Cycling performances of the symmetrical Li || Li cells with 45% IF and EC+DMC electrolytes at a current density of 0.5 mA cm^{-2} with a fixed capacity of 0.5 mAh cm^{-2} .

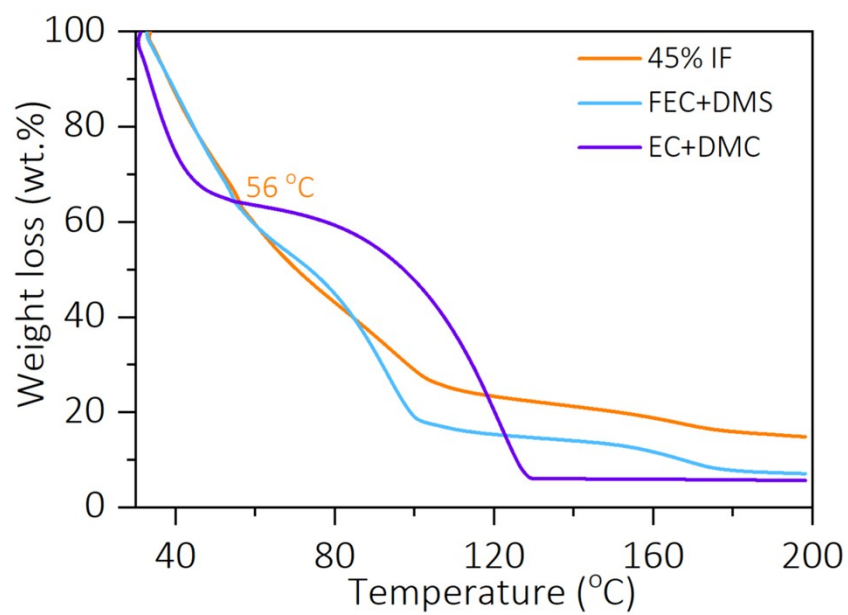


Fig. S21 Thermo-gravimetric analysis profiles of different electrolytes. The heating rate is 1 °C min⁻¹.

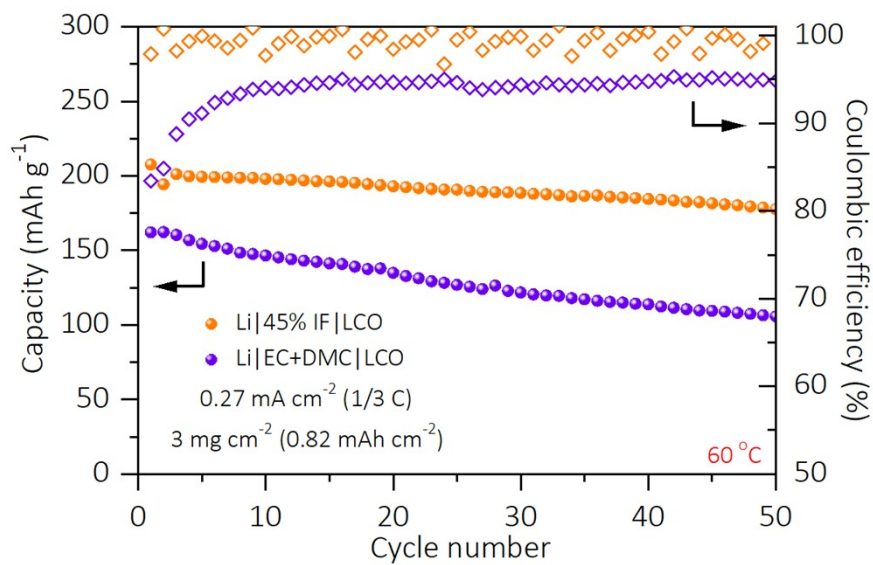


Fig.S22 Cycling performances of the Li || LCO cells with 45% IF and EC+DMC electrolytes at 1/3 C and 60 °C with a LCO loading of ~3 mg cm⁻².

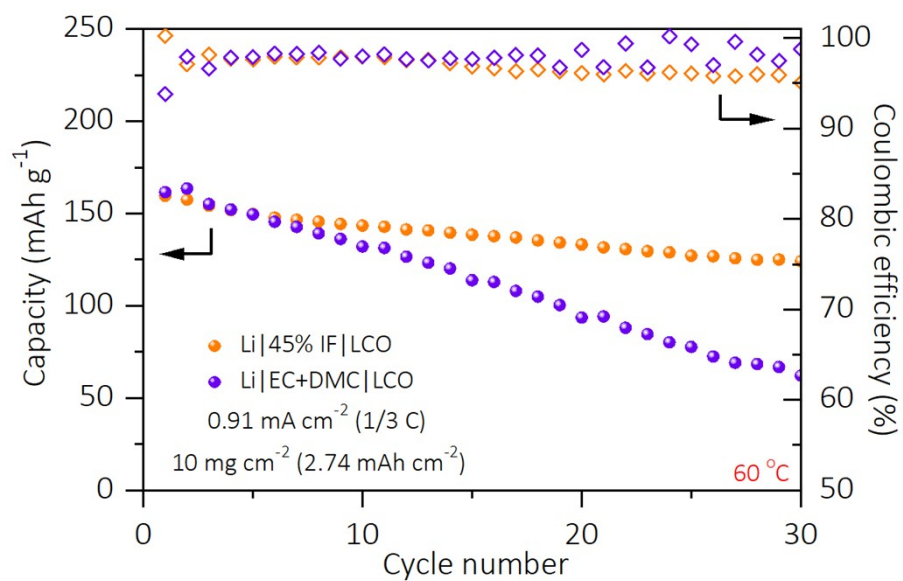


Fig. S23 Cycling performances of the Li || LCO cells with 45% IF and EC+DMC electrolytes at 1/3 C and 60 °C with a LCO loading of ~10 mg cm⁻².

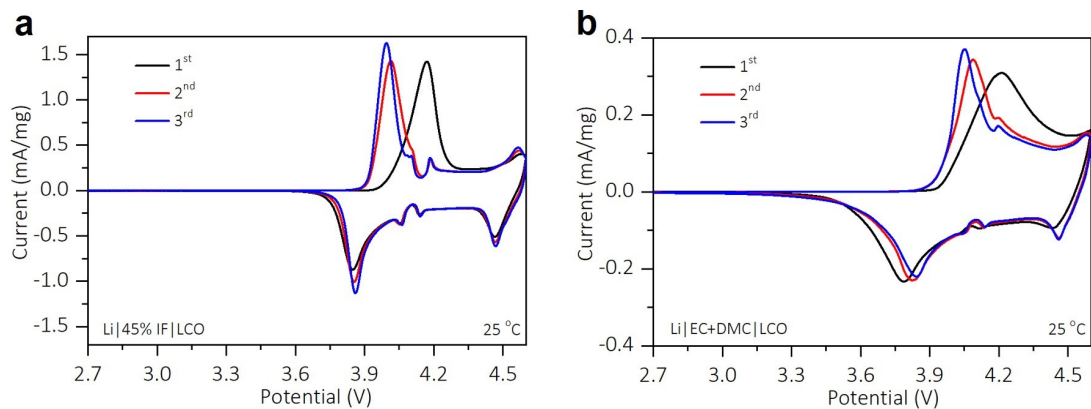


Fig. S24 CV curves of the Li || LCO cells with (a) EC+DMC and (b) 45% IF electrolytes at 25 °C.

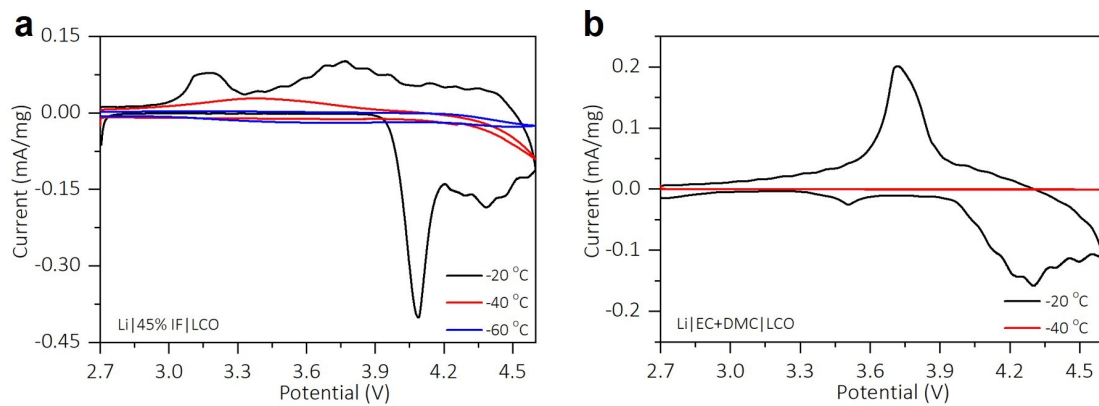


Fig. S25 CV curves of the Li || LCO cells with (a) EC+DMC and (b) 45% IF electrolytes at low temperatures.

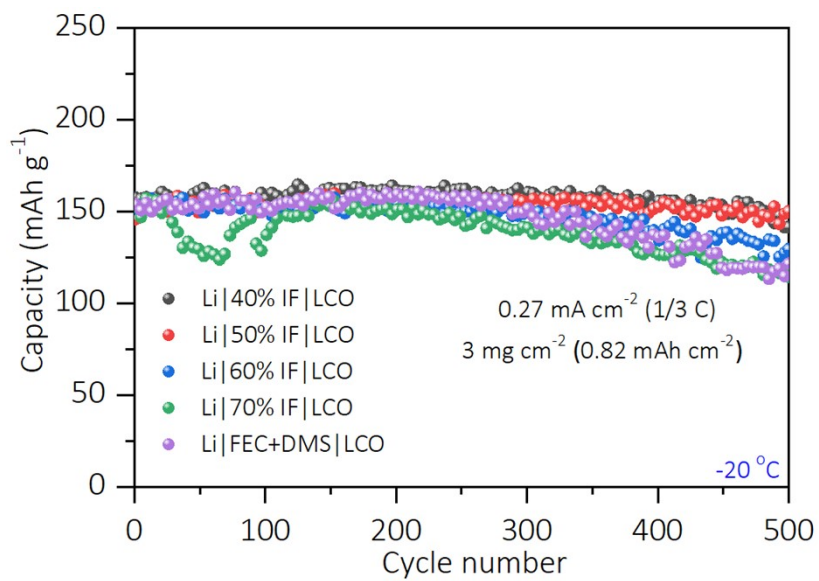


Fig. S26 Cycling performances of the Li || LCO cells with different electrolytes at 1/3 C and -20 °C.

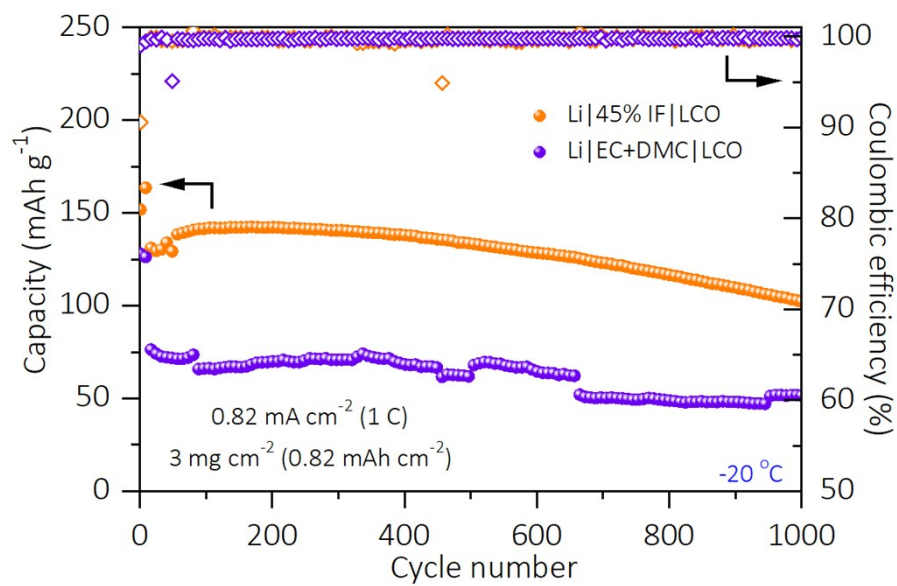


Fig. S27 Cycling performances of the Li || LCO cells with 45% IF and EC+DMC electrolytes at 1 C and $25 \text{ }^\circ\text{C}$ with a LCO loading of $\sim 3 \text{ mg cm}^{-2}$.

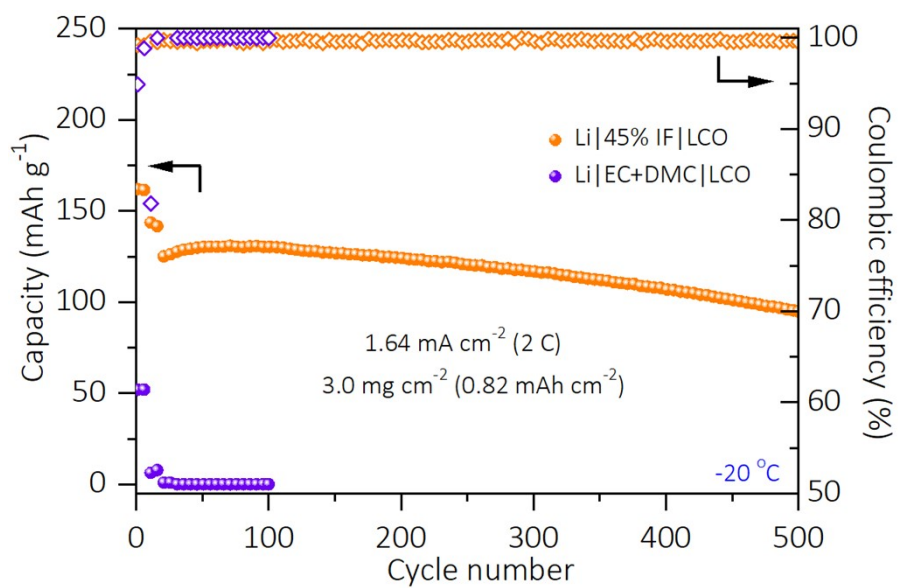


Fig. S28 Cycling performances of the Li || LCO cells with 45% IF and EC+DMC electrolytes at 2 C and 25 °C with a LCO loading of ~3 mg cm⁻².

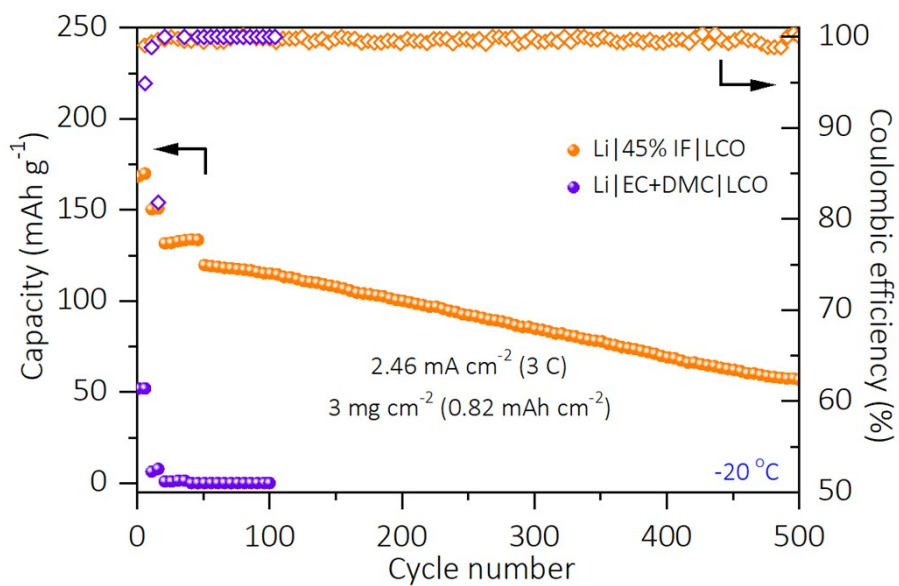


Fig. S29 Cycling performances of the Li || LCO cells with 45% IF and EC+DMC electrolytes at 3 C and 25 °C with a LCO loading of $\sim 3 \text{ mg cm}^{-2}$.

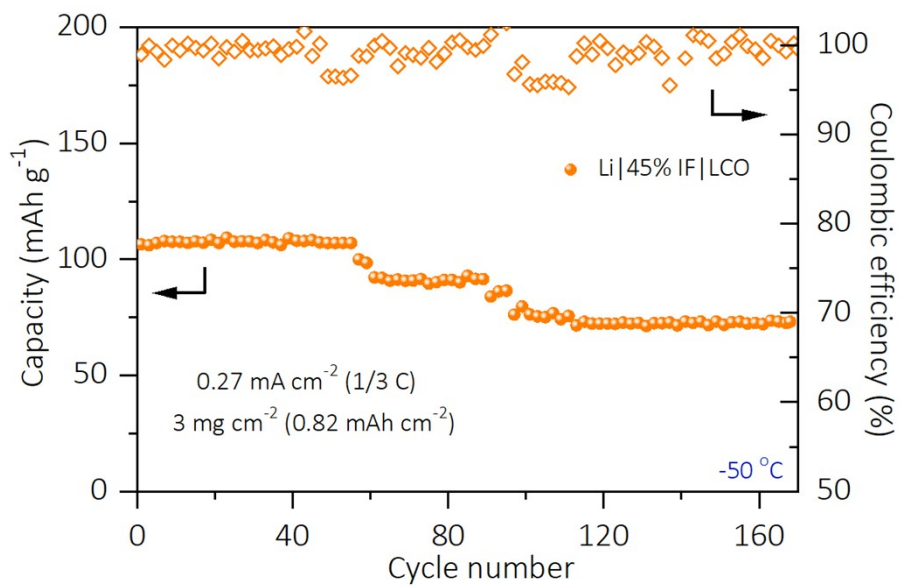


Fig. S30 Cycling performances of the Li || LCO cell with the 45% IF electrolyte at 1/3 C and -50 °C with a LCO loading of ~3 mg cm⁻².

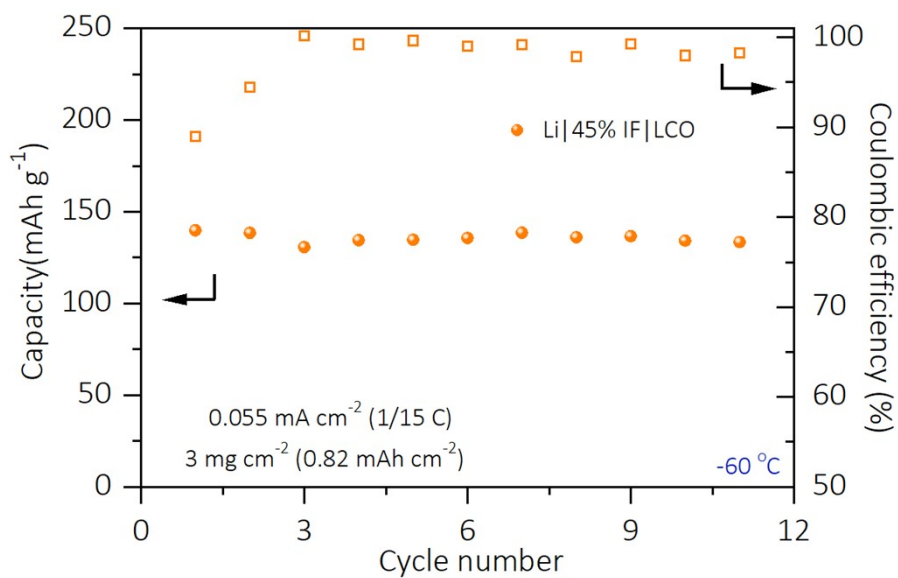


Fig. S31 Cycling performances of the Li || LCO cell with the 45% IF electrolyte at 1/15 C and -60 °C with a LCO loading of ~3 mg cm⁻².

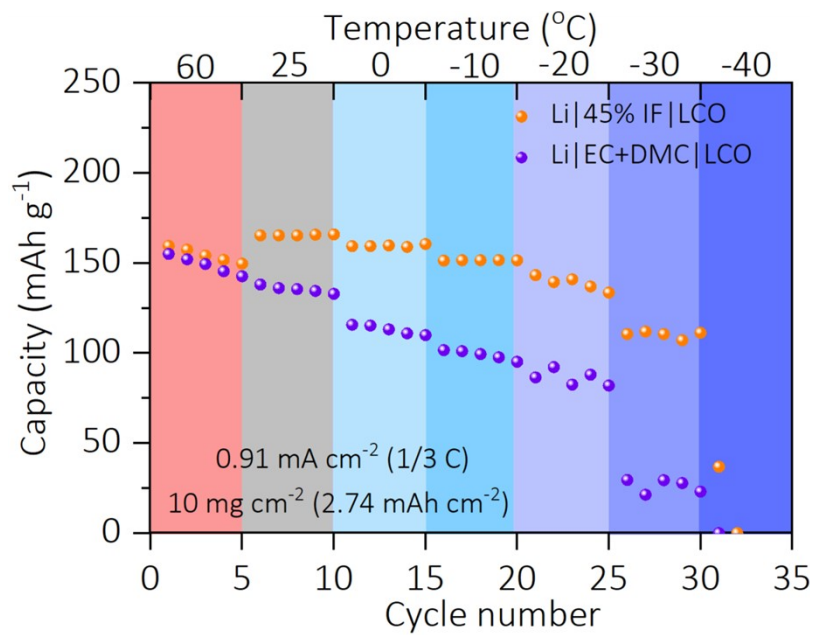


Fig. S32 Discharge capacities of the Li || LCO cells with 45% IF and EC+DMC electrolytes at different temperatures with a LCO loading of $\sim 10 \text{ mg cm}^{-2}$.

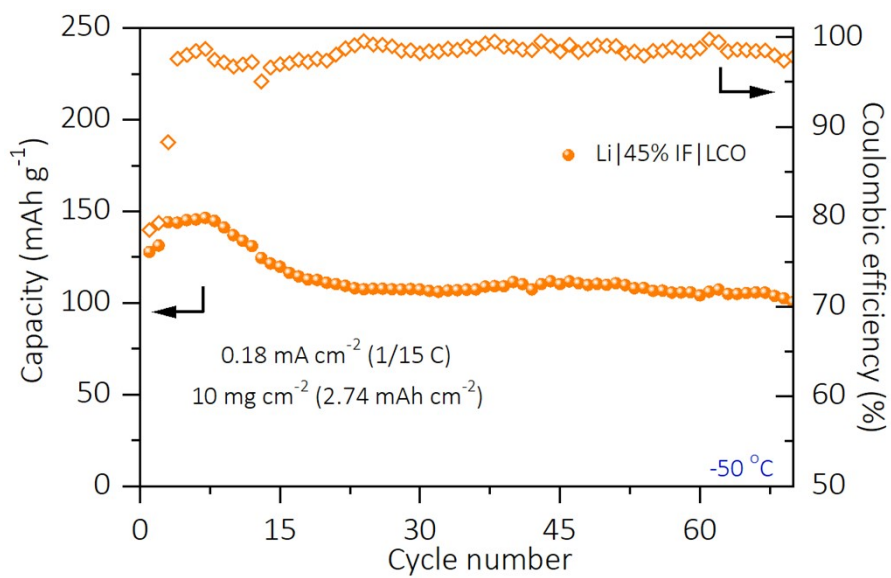


Fig. S33 Cycling performances of the Li || LCO cell with the 45% IF electrolyte at 1/15 C and -50 °C with a LCO loading of ~10 mg cm⁻².

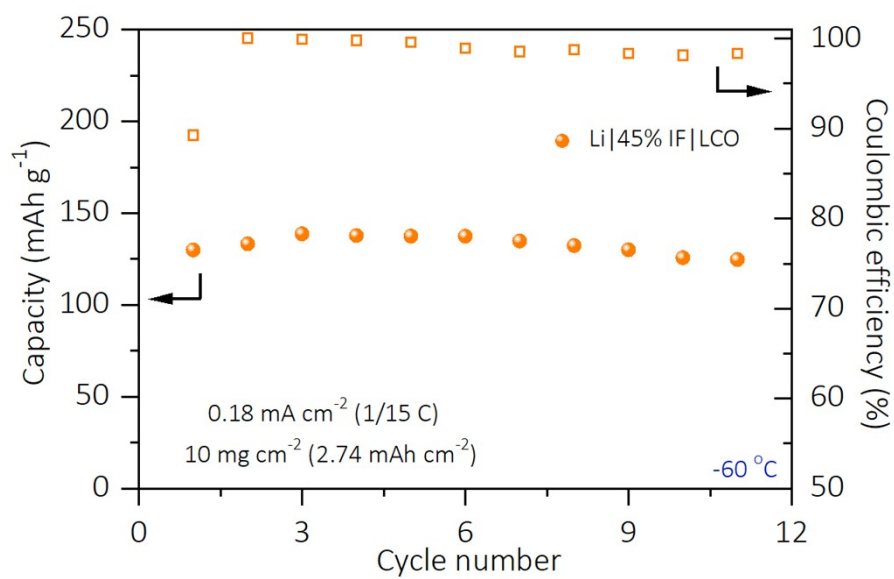


Fig. S34 Cycling performances of the Li || LCO cell with the 45% IF electrolyte at 1/15 C and -60 °C with a LCO loading of ~10 mg cm⁻².

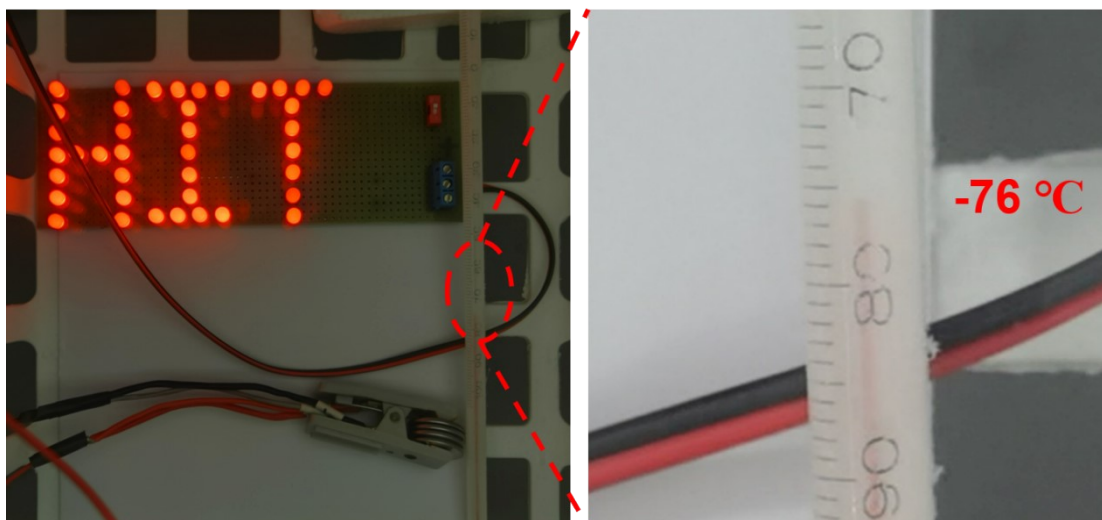


Fig. S35 Optical images of a set of led bulbs powered by the Li || LCO cells for 72 hours with the 45% IF electrolyte at $-76\text{ }^{\circ}\text{C}$.

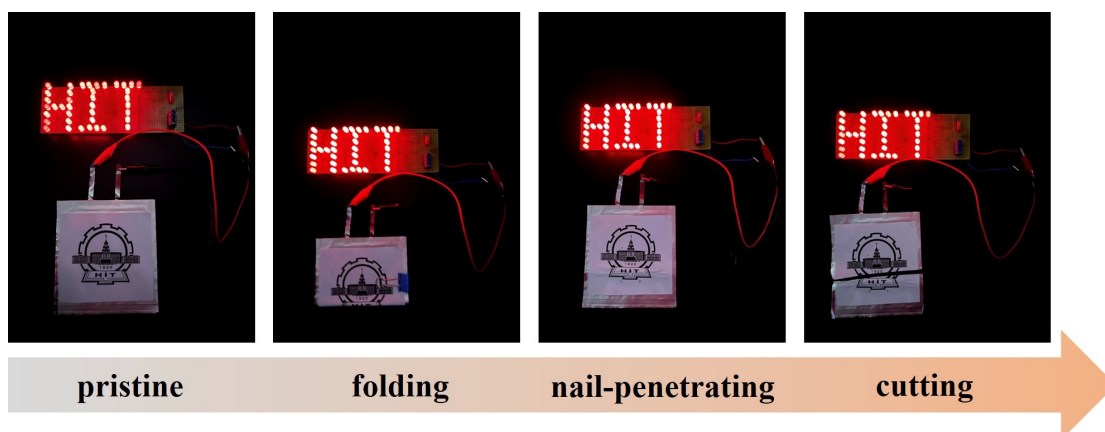


Fig. S36 Illustration of (a) pouch Li metal cells with the 45% IF electrolyte, showing normal battery operation even upon being (b) folded, (c) nail-penetrated and (d) cut.

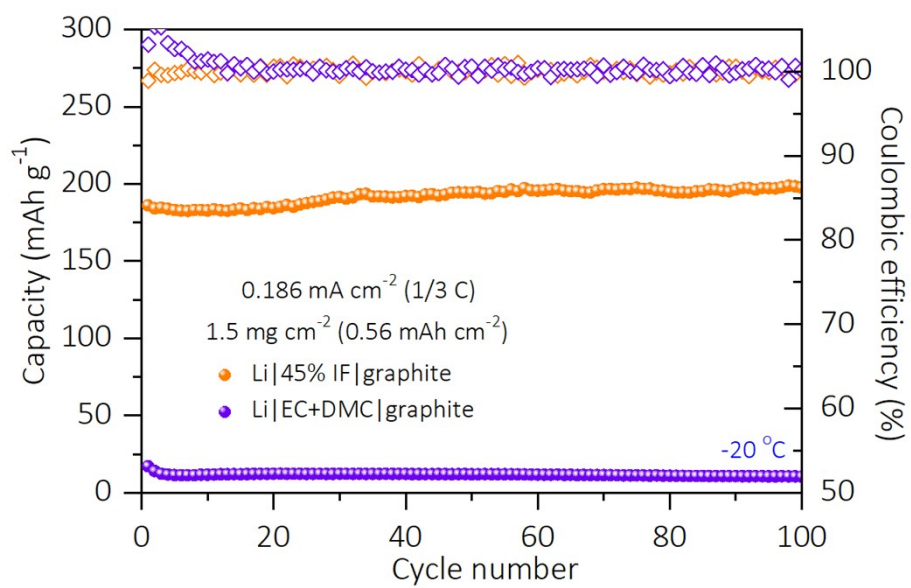


Fig. S37 Cycling performances of Li || graphite cells with different electrolytes at 1/3 C and -20 °C.

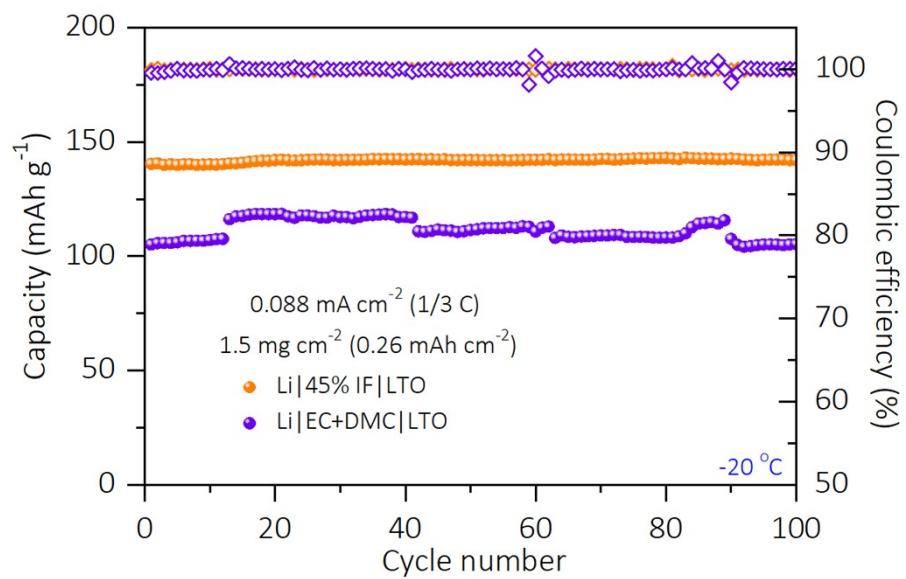


Fig. S38 Cycling performances of Li || LTO cells with different electrolytes at 1/3 C and -20 °C.

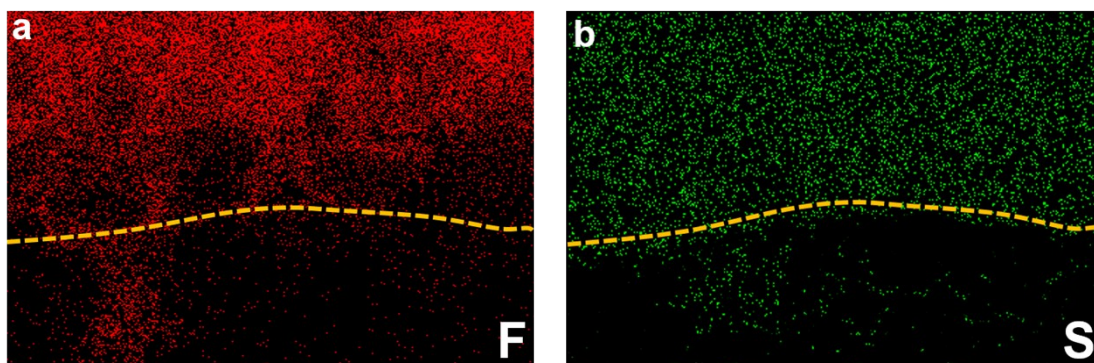


Fig. S39 Cross-view section EDS mapping of (a) F element and (b) S element of the cycled Li metal with the 45% IF electrolyte.

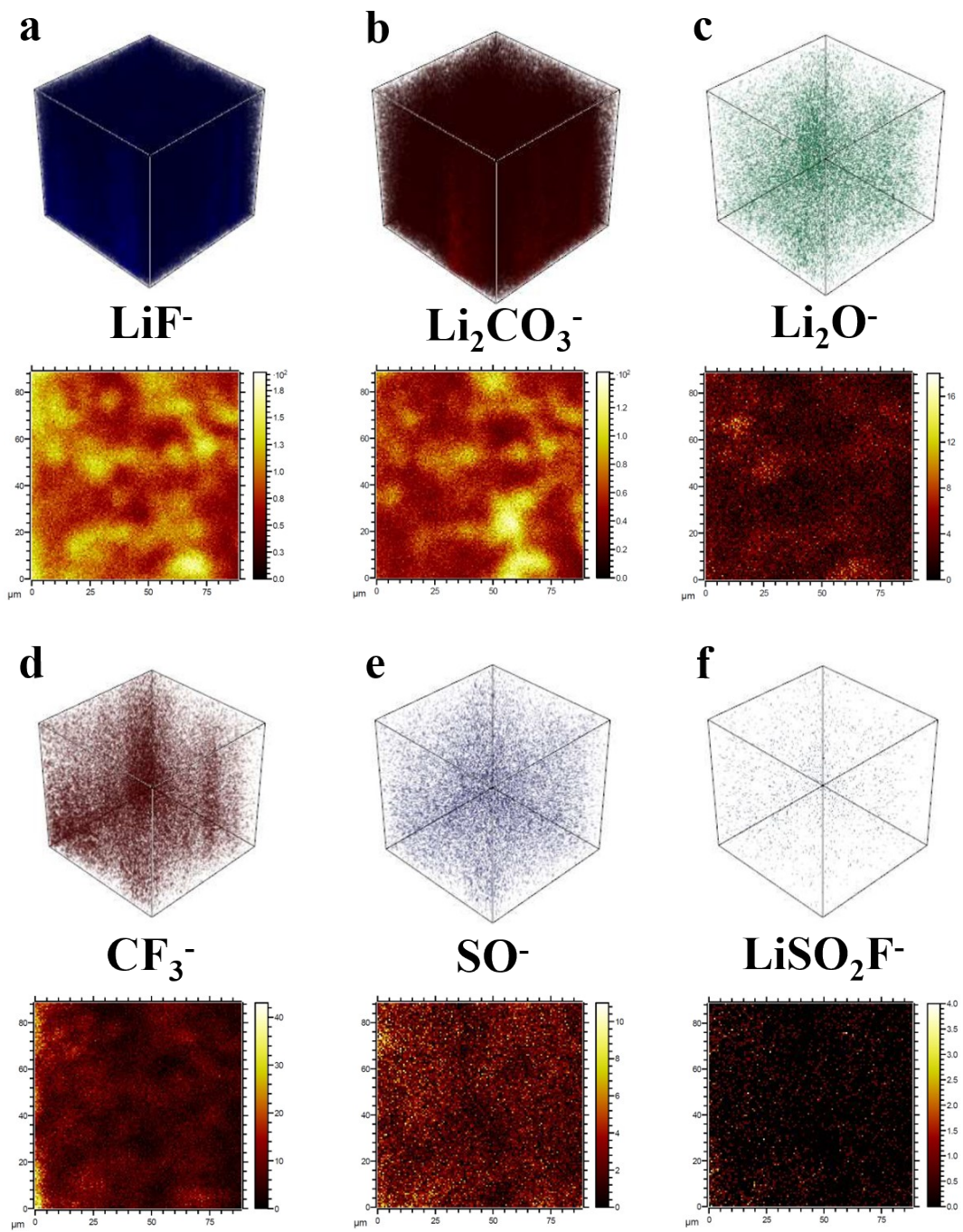


Fig. S40 TOF-SIMS three-dimensional depth images and TOF-SIMS maps of (a) LiF⁻, (b) Li₂CO₃⁻, (c) Li₂O⁻, (d) CF₃⁻, (e) SO⁻, and (f) LiSO₂F⁻.

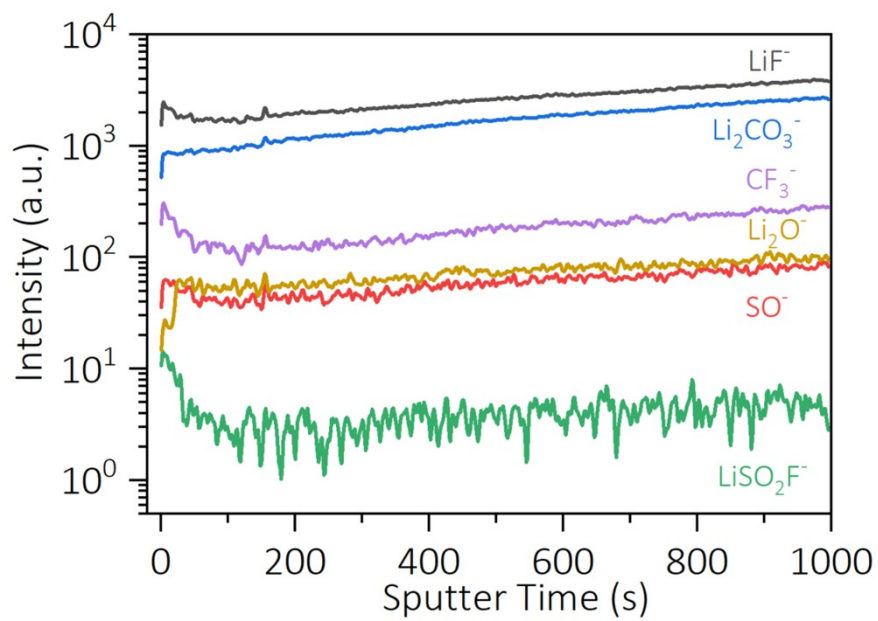


Fig. S41 TOF-SIMS depth curves of LiF^- , Li_2CO_3^- , CF_3^- , Li_2O^- , SO^- , and LiSO_2F^- species in the Li metal anode with the 45% IF electrolyte after cycling at -20°C .

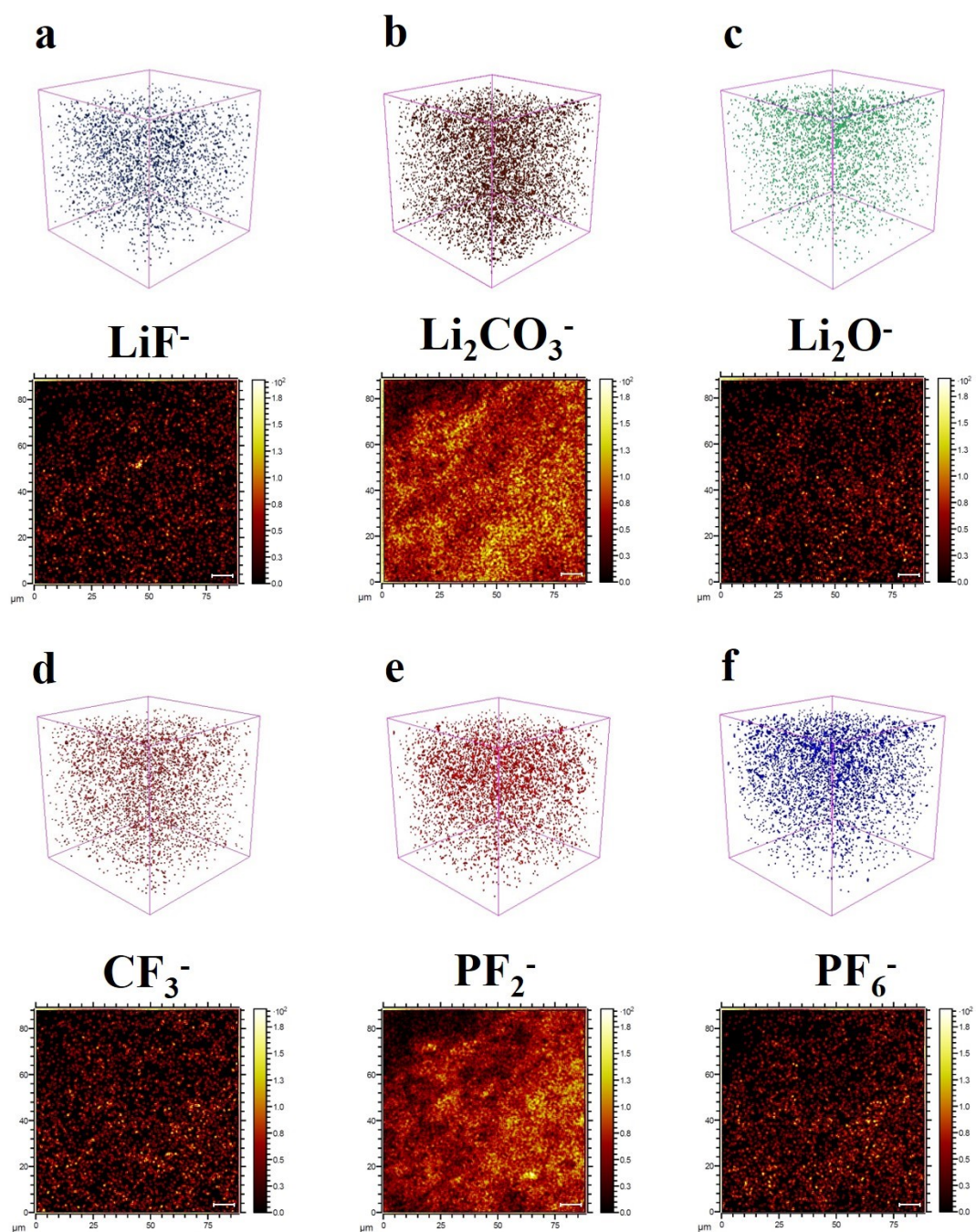


Fig. S42 TOF-SIMS three-dimensional depth images and TOF-SIMS maps of (a) LiF⁻, (b) Li₂CO₃⁻, (c) Li₂O⁻, (d) CF₃⁻, (e) PF₂⁻, and (f) PF₆⁻.

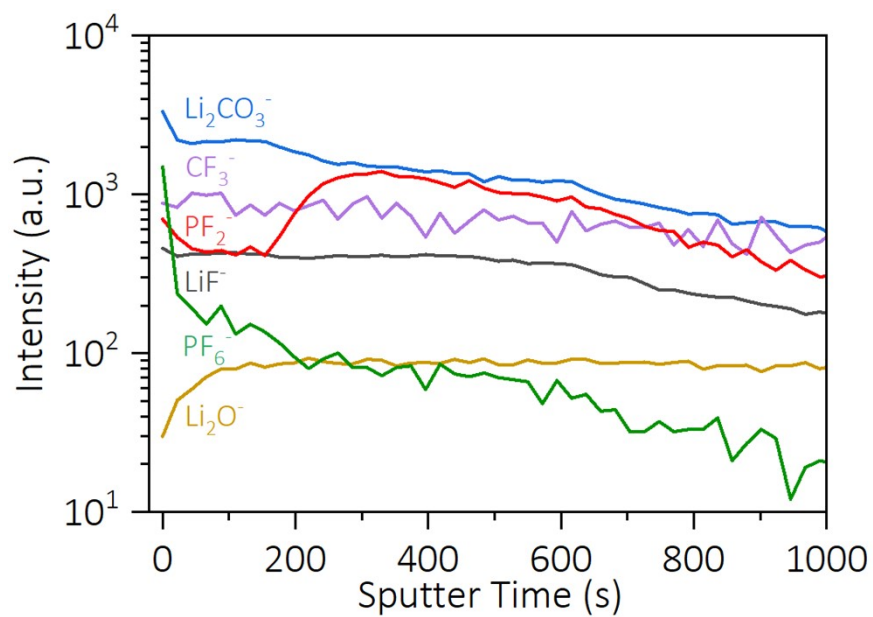


Fig. S43 TOF-SIMS depth curves of Li₂CO₃⁻, CF₃⁻, PF₂⁻, LiF⁻, PF₆⁻, and Li₂O⁻ species in the Li metal anode with the EC+DMC electrolyte after cycling at -20 °C.

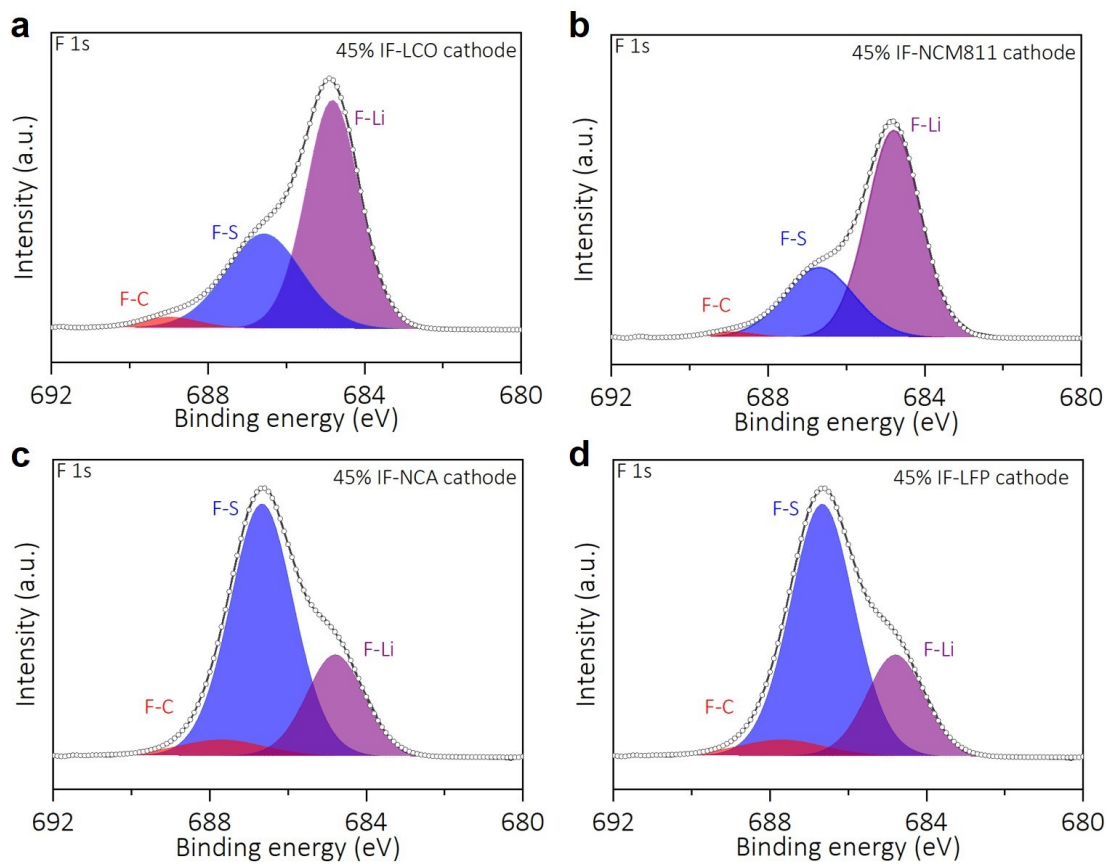


Fig. S44 XPS of F 1s spectra of the CEI interfaces for the cycled (a) LCO, (b) NCM811, (c) NCA, and (d) LFP cathodes with the 45% IF electrolyte at -20 °C.

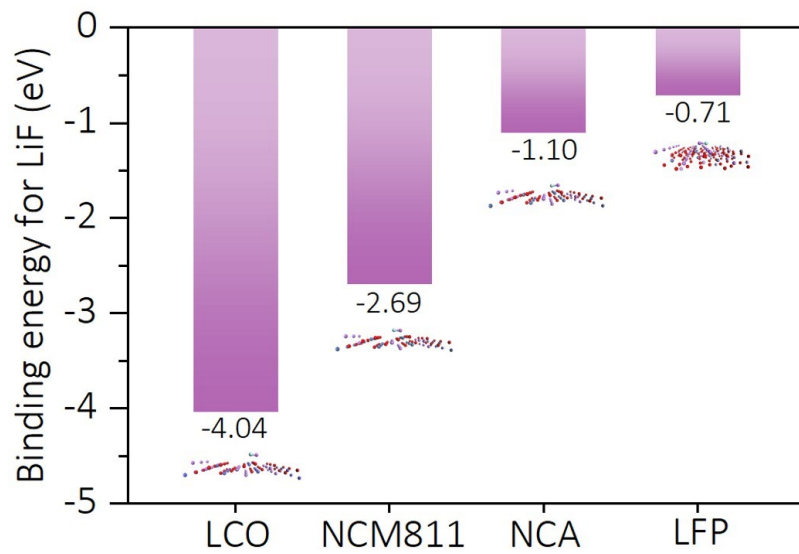


Fig. S45 Binding energy values of LiF-LCO, LiF-NCM811, LiF-NCA and LiF-LFP.

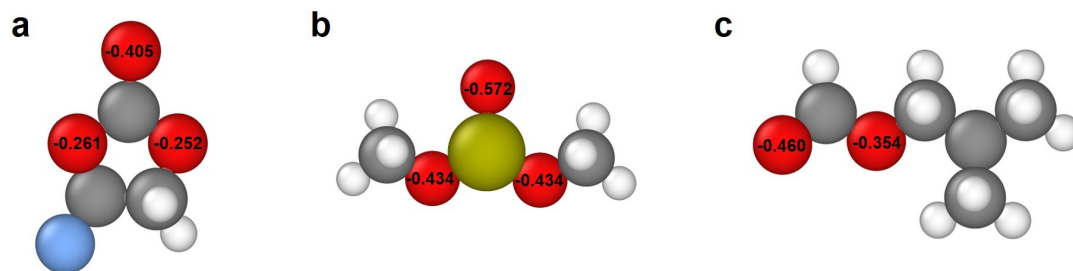


Fig. S46 The charges of oxygen atoms in (a) FEC, (b) DMS, and (c) IF.

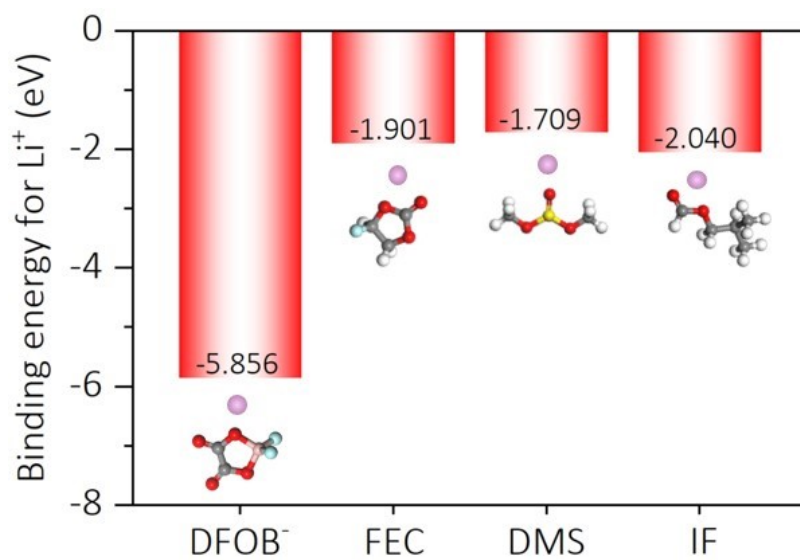


Fig. S47 Binding energy values of Li^+ - DFOB^- , Li^+ - FEC , Li^+ - DMS , and Li^+ - IF .

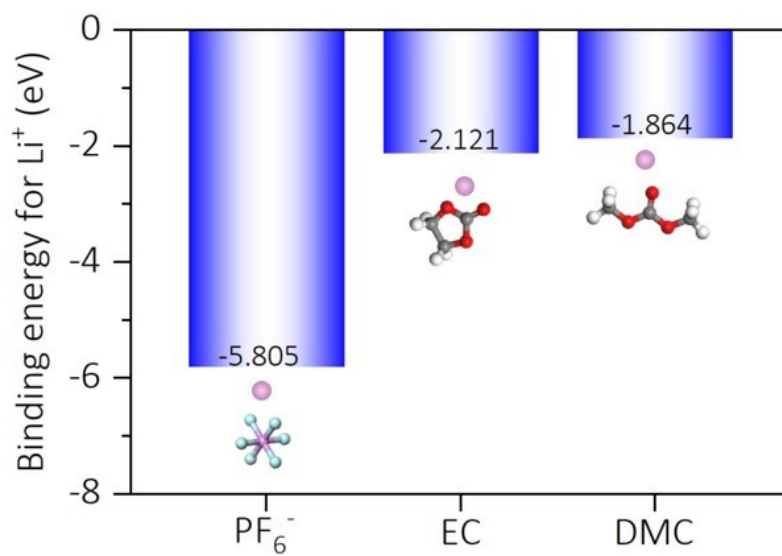


Fig. S48 Binding energy values of Li⁺-PF₆⁻, Li⁺-EC, and Li⁺-DMC.

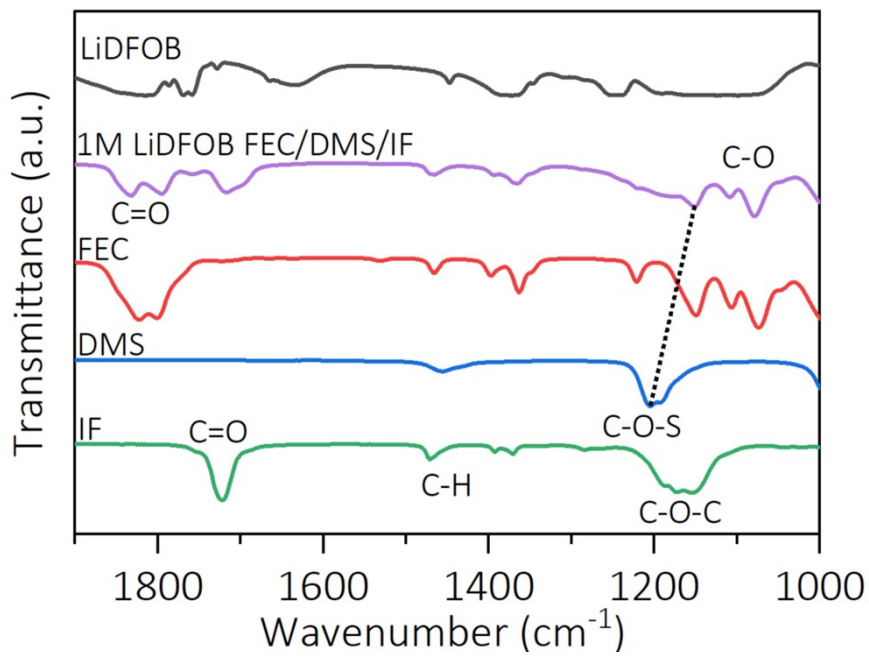


Fig. S49 FT-IR spectra obtained from the 45% IF electrolyte of interest and their components.

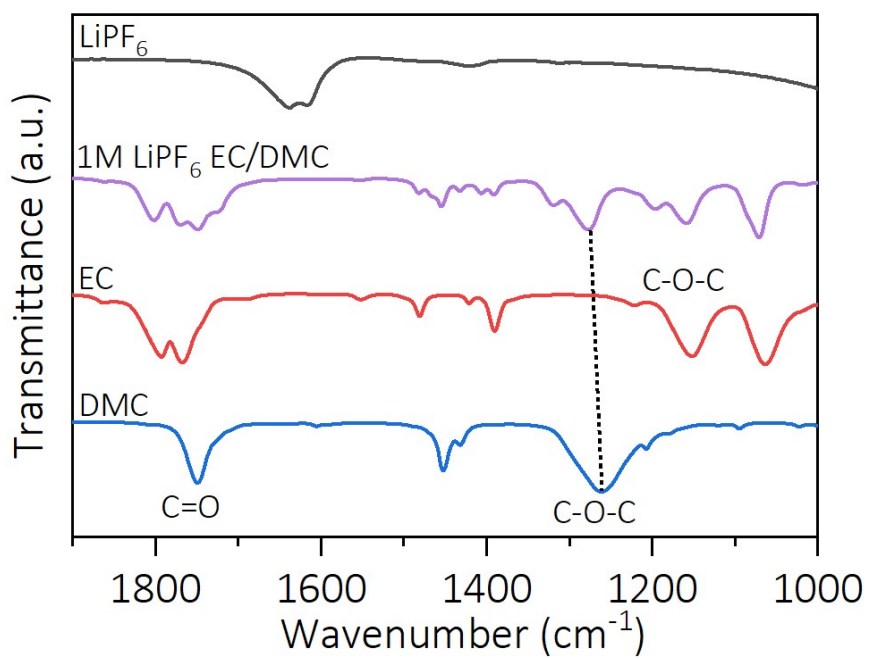


Fig. S50 FT-IR spectra obtained from the EC+DMC electrolyte of interest and their components.

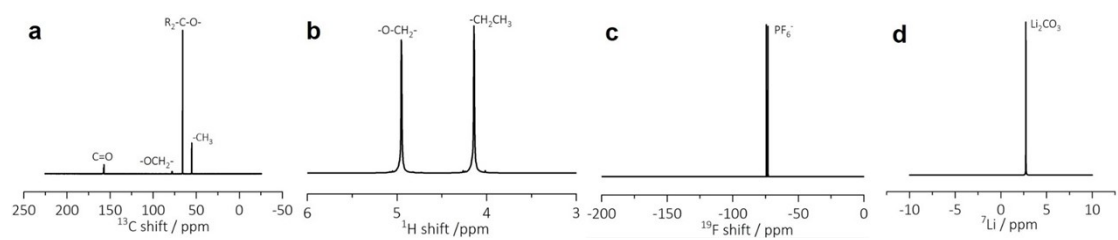


Fig. S51 (a-d) ^{13}C , ^1H , ^{19}F , and ^7Li liquid-state NMR spectra of the EC+DMC electrolyte residues after the fiftieth cycle at -20 °C.

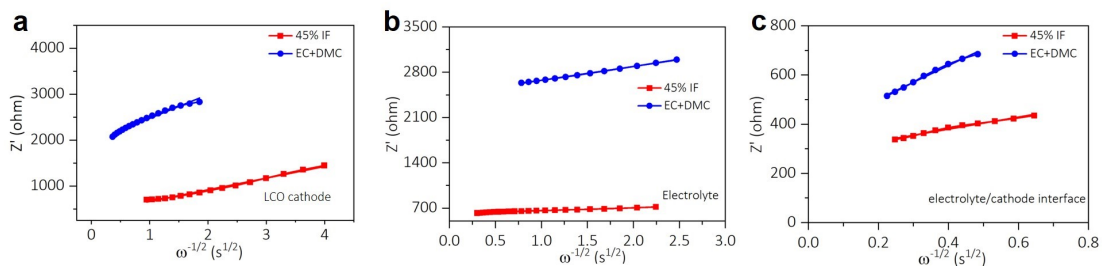


Fig. S52 (a-c) Real parts of the complex impedance versus $\omega^{-1/2}$ at LCO cathode, electrolyte, and electrolyte/cathode interface with 45% IF and EC+DMC electrolytes at $-20\text{ }^\circ\text{C}$.

Table S1 The compositions of the electrolytes investigated in this work.

Group	Key component IF (vt%)	FEC (vt%)	DMS (vt%)	EC (vt%)	DMC (vt%)	LiDFOB (mol/L)	LiPF ₆ (mol/L)	Name in our work
E1	40	20	40	/	/	1	/	40% IF
E2	45	20	35	/	/	1	/	45% IF
E3	50	20	30	/	/	1	/	50% IF
E4	60	20	20	/	/	1	/	60% IF
E5	70	20	10	/	/	1	/	70% IF
R1	/	50	50	/	/	1	/	FEC+DMS
R2	/	/	/	50	50	/	1	EC+DMC

E1-E5 are self-made electrolytes. Among them, the 45% IF electrolyte exhibits the most comprehensive electrochemical performance, as the key research object. R1 and R2 are commercial electrolytes as references.

Table S2 Coordination numbers of various low temperature electrolytes.

Electrolyte	CN	Refs
5 M LiTFSI–EA/DCM	Li-O(EA) =1.7	<i>Angew. Chem. Int. Ed.</i> 58 , 5623-5627 (2019). ¹³
2 M LiTFSI–AN/FM	Li-F(FM)=1.2, Li-N(AN)=0.8	<i>Energy Environ. Sci.</i> 13 , 2209-2219 (2020). ¹⁴
1M LiPF ₆ -MTEFP/FEC	Li-O(MTEFP) =2.7	<i>ACS Energy Lett.</i> 5 , 1438-1447 (2020). ¹⁵
1M LiTFSI-DEE	Li-O(DEE) =1.8	<i>Nat. Energy</i> 6 , 303-313 (2021). ¹⁶
1M LiTFSI-DOL/DME	Li-O(DME) =4.6	DOL+DME commercial electrolyte
1M LiPF ₆ -EC/DMC	Li-O(DMC)=3.6	EC+DMC commercial electrolyte
1M LiDFOB-FEC/DMS/IF	Li-O(IF)=0.07	45% IF

Table S3 Percentage of LiF on SEI and CEI layers of various low-temperature electrolytes.

Electrolytes	Percentage of LiF on SEI	Percentage of LiF on CEI	Refs
0.2 M LiTFSI-FM-CO ₂	20.8%	9.5%	<i>Science</i> 356 , 10 (2017). ¹⁷
1.2 M LiTFSI-AN-FM	4.32%	4.60%	<i>Energy Environ. Sci.</i> 13 , 2209-2219 (2020). ¹⁴
1 M LiPF ₆ MTFP-FEC	3.60%	2.30%	<i>ACS Energy Lett.</i> 5 , 1438-1447 (2020). ¹⁵
1M LiPF ₆ -EC-EMC-DMS	8.52%	/	<i>ACS Appl. Mater. Interfaces</i> 11 , 38285-38293 (2019). ¹⁸
EC+DMC	6.73%	6.97%	EC+DMC commercial electrolyte
45% IF	10.48%	17.91%	This work

Table S4 Ionic conductivity and diffusion coefficient of various cell components at -20 °C.

Component	EC+DMC electrolyte (-20 °C)		45% IF electrolyte (-20 °C)	
	Conductivity (mS cm ⁻¹)	Diffusion coefficient D_{Li^+} (m ² s ⁻¹)	Conductivity (mS cm ⁻¹)	Diffusion coefficient D_{Li^+} (m ² s ⁻¹)
LCO cathode	$\sim 1.10 \times 10^{-5}$ ¹⁹	4.95×10^{-21}	$\sim 1.10 \times 10^{-5}$ ¹⁹	2.21×10^{-20}
Electrolyte	3.812	4.53×10^{-21}	4.856	9.35×10^{-20}
Electrolyte/anode interface	7.53×10^{-7} ²⁰	1.24×10^{-22} ⁶	1.00×10^{-5}	1.10×10^{-21}
Electrolyte/cathode interface	4.50×10^{-5} ²¹	2.90×10^{-21}	6.65×10^{-5}	2.07×10^{-20}

Table S5 Contents of LiF in the SEIs with various electrolytes.

Composition of SEIs	LiF (%)	F-S (%)	F-P (%)	F-C (%)	LiPF ₆ (%)	Atomic concentration of F (%)	Content of LiF (%)
45% IF	54.92	39.87	-	5.21	-	19.08	10.48
EC+DMC	36.09	-	62.72		1.20	18.66	6.73

Table S6 The physical properties of various solvents.

Solvent	Boiling point (°C)	Freezing point (°C)	Flash point (°C)	Viscosity (mpa·s,20 °C)	Dielectric constant
EC	248	39	150	1.86	89.6
DMC	90	3	15	0.59	3.1
FEC	249	18	120	4.1	107
DMS	126	-114	30	0.87	22.5
IF	98	-95	21	0.68×10^{-3}	6.41

Table S7 The prices of IF agent and various fluorinated diluents.

Agent	Purity	Cost	Manufacturer	References
Isobutyl formate (IF)	97%	\$ 710.95/kg	Sigma-Aldrich	This work
1,1,1,2,2,3,3,4,4-Nonafluoro-4-methoxybutane (M3)	99%	\$ 759.27/kg	Sigma-Aldrich	22
Methyl 3,3,3-trifluoropropionate (MTFP)	98%	\$ 43493 /kg	Shanghai Macklin Biochemical Co., Ltd	15
Bis(2,2,2-trifluoroethyl) ether (BTFE)	98%	\$ 34237.35/kg	Sigma-Aldrich	23
Fluorinated borate [tri(2,2,2-trifluoroethyl) borate (TFEB)]	97%	\$ 22337.86/kg	Sigma-Aldrich	24
1,2-Difluorobenzene (1,2-dfBen)	98%	\$ 5008.85/kg	Sigma-Aldrich	25
1,1,2,2-Tetrafluoroethyl methyl ether (TFME)	98%	\$ 892.31/kg	Shanghai Aladdin Co., Ltd	26
Fluoromethyl 1,1,1,3,3,3-hexafluoroisopropyl ether (SFE)	98%	\$ 18239/kg	Shanghai Macklin Biochemical Co., Ltd	27
Either trifluoromethoxybenzene (TFMB)	99%	\$ 3174.65/kg	Sigma-Aldrich	28
Tris(2,2,2-trifluoroethyl) orthoformate (TFEO)	97%	\$ 404064/kg	Alfa Chemistry	29

Table S8 The low temperature performance compared with recent reports.

Electrolyte	Electrode	Loading (mg cm ⁻²)	-20 °C Performance			Ultra-low temperature performance			Refs
			Rate (C)	Capacity (mAh g ⁻¹)	Cycle number	Rate (C)	Capacity (mAh g ⁻¹)	Cycle number	
1.28 M LiFSI-FEMC/FEC in D2	Li/NCA	4	1/3	150	450	1/15	96 (charged at room temperature, discharged at -85 °C)	1	<i>Nat. Energy</i> 4 , 882-890 (2019). ²²
2 M LiTFSI-AN/FM	Li/NMC622	6.4	1/3	120	300	1/15	85 (charged and discharged at -60 °C)	1	<i>Energy Environ. Sci.</i> 13 , 2209- 2219 (2020). ¹⁴
0.2 M LiTFSI-FM/CO ₂	Li/LCO	6.6	1/10	132 (-10 °C)	5	1/10	83 (charged and discharged at -60 °C)	5	<i>Science</i> 356 , 10 (2017). ¹⁷
1 M LiPF ₆ -EC/DMC	Li/LiF-coated NCM	3.2	1/10	135	10	1/10	105 (charged and discharged at -30 °C)	10	<i>J. Mater. Chem. A</i> 7 , 11513-11519 (2019). ³⁰

5 M LiTFSI-EA/DCM	Li/Nb ₂ O ₅	1	/	/	1/2	90 (charged and discharged at -75 °C)	100	<i>Batteries Supercaps</i> 3 , 1016-1020 (2020). ³¹ <i>Angew. Chem. Int. Ed.</i> 58 , 5623-5627 (2019). ¹³
5 M LiTFSI-EA/DCM	Li/PI	2	/	/	1/5	70 (charged and discharged at -70 °C)	100	<i>Adv. Sci.</i> 7 , 8 (2020). ³²
5 M LiTFSI-EA/DCM	Li/NiHCF	1-2	1/20	66 (-25 °C)	1	59 (charged and discharged at -70 °C)	1	<i>ACS Energy Lett.</i> 5 , 1438-1447 (2020). ¹⁵
1M LiPF ₆ -MTFP/FEC	Li/NCM811	6.5	1/10	161(charged at room temperature, discharge at -40 °C)	1	133 (charged at room temperature, discharged at -60 °C)	1	<i>Nat. Energy</i> 6 , 303-313 (2021). ¹⁶
1M LiTFSI-DEE	Li/SPAN	2	/	/	/	120 (charged and discharged at -60 °C)	50	<i>Adv. Energy Mater.</i> 3 , 1155-1160 (2013). ³³
1M LiPF ₆ -EC/DMC/DMC	Li/LFP@C	~2	1/5	-25	1	/	/	

45%IF	Li/LCO	10	1/3	80	200	1/15	90 (charged and discharged at -70 °C)	40	Our work
45%IF	Li/LCO	3	1/3	156	500	1/15	115 (charged and discharged at -70 °C)	170	Our work

Table S9 LiF atomic concentration of CEI on different cathode materials.

CEI	F 1s atomic concentration (%)	LiF area (%)	LiF atomic concentration (%)
LCO	29.32	61.08	17.91
NCM81 1	21.39	68.32	14.61
NCA	13.26	25.29	3.35
LFP	13.97	1.48	0.21

Table S10 The lattice misfit between LiF and different cathode materials.

Crystal	a (Å)	b (Å)	c (Å)	Space group	Lattice misfit with LiF
LiF	2.56	2.56	2.56	Pm $\bar{3}$ m	/
LCO	2.814	2.814	14.048	R $\bar{3}$ m	9.92%
NCM811	2.8645	2.8645	14.161	R $\bar{3}$ m	11.89%
NCA	2.86	2.86	14.199	R $\bar{3}$ m	11.72%
LFP	4.746	10.444	6.090	Pnma	85.39%

References:

- 1 E. P. Wohlfarth, *Phys. Lett. A*, 1979, **70**, 489-491.
- 2 S. Zugmann, M. Fleischmann, M. Amereller, R. M. Gschwind, H. D. Wiemhofer and H. J. Gores, *Electrochim. Acta*, 2011, **56**, 3926-3933.
- 3 N. Takami, A. Satoh, M. Hara and I. Ohsaki, *J. Electrochem. Soc.*, 1995, **142**, 371-379.
- 4 S. L. Chou, J. Z. Wang, H. K. Liu and S. X. Dou, *J. Phys. Chem. C*, 2011, **115**, 16220-16227.
- 5 B. H. Li, C. P. Han, Y. B. He, C. Yang, H. D. Du, Q. H. Yang and F. Y. Kang, *Energy Environ. Sci.*, 2012, **5**, 9595-9602.
- 6 P. J. Guan, L. Liu and X. K. Lin, *J. Electrochem. Soc.*, 2015, **162**, A1798-A1808.
- 7 W. L. Jorgensen, D. S. Maxwell and J. TiradoRives, *J. Am. Chem. Soc.*, 1996, **118**, 11225-11236.
- 8 W. Damm, A. Frontera, J. TiradoRives and W. L. Jorgensen, *J. Comput. Chem.*, 1997, **18**, 1955-1970.
- 9 L. S. Dodda, I. C. de Vaca, J. Tirado-Rives and W. L. Jorgensen, *Nucleic Acids Res.*, 2017, **45**, W331-W336.
- 10 L. S. Dodda, J. Z. Vilseck, J. Tirado-Rives and W. L. Jorgensen, *J. Phys. Chem. B*, 2017, **121**, 3864-3870.
- 11 J. N. C. Lopes and A. A. H. Padua, *J. Phys. Chem. B*, 2004, **108**, 16893-16898.
- 12 L. Martinez, R. Andrade, E. G. Birgin and J. M. Martinez, *J. Comput. Chem.*, 2009, **30**, 2157-2164.
- 13 X. L. Dong, Y. X. Lin, P. L. Li, Y. Y. Ma, J. H. Huang, D. Bin, Y. G. Wang, Y. Qi and Y. Y. Xia, *Angew. Chem. Int. Ed.*, 2019, **58**, 5623-5627.
- 14 Y. Y. C. Yang, Y. J. Yin, D. M. Davies, M. H. Zhang, M. Mayer, Y. H. Zhang, E. S. Sablina, S. Wang, J. Z. Lee, O. Borodin, C. S. Rustomji and Y. S. Meng, *Energy Environ. Sci.*, 2020, **13**, 2209-2219.
- 15 J. Holoubek, M. Y. Yu, S. C. Yu, M. Q. Li, Z. H. Wu, D. W. Xia, P. Bhaladhare, M. S. Gonzalez, T. A. Pascal, P. Liu and Z. Chen, *ACS Energy Lett.*, 2020, **5**, 1438-1447.
- 16 J. Holoubek, H. Liu, Z. Wu, Y. Yin, X. Xing, G. Cai, S. Yu, H. Zhou, T. A. Pascal, Z. Chen and P. Liu, *Nat. Energy*, 2021, **6**, 303-313.
- 17 C. S. Rustomji, Y. Yang, T. K. Kim, J. Mac, Y. J. Kim, E. Caldwell, H. Chung and S. Meng, *Science*, 2017, **356**, eaal4263.
- 18 R. D. Guo, Y. X. Che, G. Y. Lan, J. L. Lan, J. H. Li, L. D. Xing, K. Xu, W. Z. Fan, L. Yu and W. S. Li, *ACS Appl. Mater. Interfaces*, 2019, **11**, 38285-38293.
- 19 S. Y. Wang, M. Y. Yan, Y. Li, C. Vinado and J. H. Yang, *J. Power Sources*, 2018, **393**, 75-82.
- 20 B. Han, D. Y. Feng, S. Li, Z. Zhang, Y. C. Zou, M. Gu, H. Meng, C. Y. Wang, K. Xu, Y. S. Zhao, H. B. Zeng, C. S. Wang and Y. H. Deng, *Nano Lett.*, 2020, **20**, 4029-4037.
- 21 F. L. Zhang, C. Wang, D. N. Zhao, L. Yang, P. Wang, W. B. Li, B. Wang and S. Y. Li, *Electrochim. Acta*, 2020, **337**, 135727.

- 22 X. L. Fan, X. Ji, L. Chen, J. Chen, T. Deng, F. D. Han, J. Yue, N. Piao, R. X. Wang, X. Q. Zhou, X. Z. Xiao, L. X. Chen and C. S. Wang, *Nat. Energy*, 2019, **4**, 882-890.
- 23 S. R. Chen, J. M. Zheng, L. Yu, X. D. Ren, M. H. Engelhard, C. J. Niu, H. Lee, W. Xu, J. Xiao, J. Liu and J. G. Zhang, *Joule*, 2018, **2**, 1548-1558.
- 24 X. Cao, P. Y. Gao, X. D. Ren, L. F. Zou, M. H. Engelhard, B. E. Matthews, J. T. Hu, C. J. Niu, D. Y. Liu, B. W. Arey, C. M. Wang, J. Xiao, J. Liu, W. Xu and J. G. Zhang, *Proc. Natl. Acad. Sci. U. S. A.*, 2021, **118**, e2020357118.
- 25 D. J. Yoo, S. Yang, K. J. Kim and J. W. Choi, *Angew. Chem. Int. Ed.*, 2020, **59**, 14869-14876.
- 26 T. T. Feng, G. Z. Yang, S. Zhang, Z. Q. Xu, H. P. Zhou and M. Q. Wu, *Chem. Eng. J.*, 2022, **433**, 134138.
- 27 C. Y. Chang, Y. Yao, R. R. Li, Z. F. Cong, L. W. Li, Z. H. Guo, W. G. Hu and X. Pu, *J. Mater. Chem. A*, 2022, **10**, 9001-9009.
- 28 C. N. Zhu, C. C. Sun, R. H. Li, S. T. Weng, L. W. Fan, X. F. Wang, L. X. Chen, M. Noked and X. L. Fan, *ACS Energy Lett.*, 2022, **7**, 1338-1347.
- 29 Y. Zheng, F. A. Soto, V. Ponce, J. M. Seminario, X. Cao, J. G. Zhang and P. B. Balbuena, *J. Mater. Chem. A*, 2019, **7**, 25047-25055.
- 30 X. Ding, Y. X. Li, F. Chen, X. D. He, A. Yasmin, Q. Hu, Z. Y. Wen and C. H. Chen, *J. Mater. Chem. A*, 2019, **7**, 11513-11519.
- 31 X. L. Dong, Y. Yang, P. L. Li, Z. Fang, Y. G. Wang and Y. Y. Xia, *Batteries Supercaps*, 2020, **3**, 1016-1020.
- 32 X. L. Dong, Y. Yang, B. L. Wang, Y. J. Cao, N. Wang, P. L. Li, Y. G. Wang and Y. Y. Xia, *Adv. Sci.*, 2020, **7**, 2000196.
- 33 X. L. Wu, Y. G. Guo, J. Su, J. W. Xiong, Y. L. Zhang and L. J. Wan, *Adv. Energy Mater.*, 2013, **3**, 1155-1160.